2019

Simulation of droplet impacting a square solid obstacle in microchannel with different wettability by using high density ratio pseudopotential multiplerelaxation- time (MRT) lattice Boltzmann Method (LBM)

Wandong Zhao
Nanchang University

Ying Zhang
Nanchang University

Wenqiang Shang
Nanchang University

Zhaotai Wang

Ben Xu
The University of Texas Rio Grande Valley, ben.xu@utrgv.edu

Recommended Citation
Wandong Zhao, Ying Zhang, Wenqiang Shang, Zhaotai Wang, Ben Xu, and Shuisheng Jiang. Simulation of droplet impacting a square solid obstacle in microchannel with different wettability by using high density ratio pseudopotential multiple-relaxation-time (MRT) lattice Boltzmann method (LBM). Canadian Journal of Physics. 97(1): 93-113. https://doi.org/10.1139/cjp-2018-0126

Simulation of droplet impacting a square solid obstacle in microchannel with different wettability by using high density ratio pseudopotential multiple-relaxation-time (MRT) lattice Boltzmann Method (LBM)

Wandong Zhao[1], Ying Zhang[1], Wenqiang Shang[1], Zhaotai Wang[1], Ben Xu[2*], Shuisheng Jiang[1]*

1. School of Mechanical and Electrical Engineering, Nanchang University, Nanchang, Jiangxi, 330031, China

2. Department of Mechanical Engineering, University of Texas Rio Grande Valley, Edinburg, TX, 78539, USA

***Corresponding authors**

Tel: +86 (791) 83969634; Email: yzhan@ncu.edu.cn (Ying Zhang)

Tel: +1 (956)665-2896; Email: ben.xu@utrgv.edu (Ben Xu)

Abstract: In this paper, a pseudopotential high density ratio (DR) lattice Boltzmann Model was developed by incorporating multi-relaxation-time (MRT) collision matrix, large DR external force term, surface tension adjustment external force term and solid-liquid pseudopotential force. It was found that the improved model can precisely capture the two-phase interface at high DR. Besides, the effects of initial Reynolds number, Weber number, solid wall contact angle (CA), ratio of obstacle size to droplet diameter (χ_1), ratio of channel width to droplet diameter (χ_2) on the deformation and breakup of droplet when impacting on a square obstacle were investigated. The results showed that with the Reynolds number increasing, the droplet will fall along the obstacle and then spread along both sides of the obstacle. Besides, by increasing Weber number, the breakup of the liquid film will be delayed and the liquid film will be stretched to form an elongated ligament. With decreasing of the wettability of solid particle (CA $\rightarrow$ 180°), the droplet will surround the obstacle and then detach from the obstacle. When χ_1 is greater than 0.5, the droplet will spread along both sides of the obstacle quickly; otherwise, the droplet will be ruptured earlier. Furthermore, when χ_2 decreases, the droplet will spread earlier and then fall along the wall more quickly; otherwise, the droplet will expand along both sides of the obstacle. Moreover, increasing the hydrophilicity of the microchannel, the droplet will impact the channel more rapidly and infiltrate the wall along the upstream and downstream simultaneously; on the contrary, the droplet will wet downstream only.

Keywords: pseudopotential; high density ratio; multiple-relaxation-time (MRT); lattice Boltzmann model (LBM); contact angle; droplet impacting on solid obstacles; microchannels.

1. Introduction

Droplets impacting solid obstacles in microchannel is a popular phenomenon in many natural phenomena, chemical processes(e.g., the separation of droplet in the pharmaceutical process) and engineering applications(e.g., the induced movement of droplet in the microfluidic devices and the collision of droplet in the combustion engine) [1, 2]. Therefore, it is always of great interests to study the geometrical and physical dynamic changes of the droplet during the collision.

Most of the phenomena that droplets hit on a solid obstacle can be divided into the level of the droplets impacting horizontal wall [3-6], spherical surface [7, 8] and inclined wall [9, 10]. If the size and shape of solid obstacles are taken into account, solid obstacles can be categorized as spherical obstacles [7, 8, 11] , cylindrical obstacles and rectangular obstacles [12-14]. Significant amount of researches have been reported to explore the characteristics of spreading, wetting, spattering, crushing, consequent pressure change and velocity change when droplet impacting on the solid obstacle through theoretical analysis, experimental study and numerical simulation.

Recently, Josserand and Thoroddsen [15] summarized the process of a droplet impacting on solid surfaces theoretically and experimentally. In their paper, they mainly explained some physical factors that control the droplet's impact on solid, such as the inertial force, the viscosity and the surface tension of the fluid. At the same time, they also revealed that the gas beneath the droplet was also a key factor for droplet splashing. However, the wall with different roughness, hydrophilicity and hydrophobicity could guide and dampen the droplet impacting process. Banitabaei and amirfazli [16] experimentally studied on droplet impact on spherical solid obstacles via experiments using high-speed cameras. The wetting characteristics of the wall were mainly taken into account and they selected three spherical obstacles with different wetting surfaces (contact angle (CA)=70°, 90°, 118°) when the droplet impact on the spherical wall. At the same time, they also extended the Weber (We) number to 1146, and they found that at large We number, as the wettability of the wall enhanced, the time it took for the droplet to be ruptured would increase for hydrophilic walls; while for the hydrophobic wall, the lamella formation of the droplet would just change a little as the contact angle increased to 110 °. Besides, their results showed that when We number is small, the droplet will not be ruptured, but falls along the spherical obstacles, and when the We number is increased to 200, the liquid film will be formed. Bakshi *et al.* [11] experimentally and theoretically investigated the dynamic behaviors of the droplet impacting on the spherical surface. They mainly researched on different ratios of droplet-to-spherical size and found that the outcomes of the droplet impacting the wall can be divided into the initial deformation stage, the inertia force stage and the viscous force stage according to the droplet morphological changes. Liang *et al.* [14] performed an experimental investigation on the droplet colliding on the cylindrical surface and mainly studied the effect of the curvature of the cylindrical surface on droplet splashing at a large We number. Stevens *et al.* [17] experimentally studied the sputtering process of low-viscosity and high-viscosity droplet impacting the plane, and their results showed that the gas pressure around the droplet greatly affects the droplet impacting, increasing the pressure of droplet, and forming a thin sheet. Antonini *et al.* [18] experimentally demonstrated that water droplets impinged on different wetting walls, and their results showed that the maximum spreading radius and wetting time of droplets were affected by the wetting characteristics when the We number was in the range of 30-200. However, when the We number is more than 200, the wetting characteristics would not be the primary factor.

Lots of prior literature experimentally investigated the effects of wetting characteristic, We number and the size of solid particle. However, the time and length scale involving in the impacting process is very small, and the environmental

variables are very difficult to control in the experimental process, such as the consistency of the droplet shape with high velocity, the selection range of the wetting property of the solid surface, the effect of gravity, *et al.* On the other hand, numerical simulation could easily study the dynamics characteristics of droplet impact on solid barriers under certain conditions. Therefore, a large number of scholars developed numerical models to investigate the droplet impacting process.

Some scholars studied the droplet impact on solid obstacles from the perspective of solving macroscopic Naiver-Stokes (N-S) via the marker-and-cell (MAC) method, volume of fluid (VOF) method, front-tracking-method (FTM), particle method and level set coupled VOF method [7, 13, 19, 20]. Pasandideh-Fard *et al.* [12] performed a numerical simulation on the dropping of the droplet along different sizes of cylindrical solid, and they found that as the solid diameter of the cylinder decreased to 0.5-1 millimeters, the size of droplet remaining on the solid became smaller and smaller, while the drop impact process would become more and more unstable. Recently, Liu *et al.* [13] performed a numerical study on the kinetics process of droplet impacting hydrophobic tubes by using a coupled level set method and VOF method. They found that, under the same CA, as the droplet impact velocity increasing, the liquid film would rebound from the solid wall earlier. Recently, Gotoh and Khayyer [21] systematically reviewed the applications of particle methods in coastal and ocean engineering, and the latest advancement included accuracy, stability multi-physics multi-scale simulations, and the authors concluded that further rigorous and comprehensive investigations must be conducted on the convergence, consistency and energy conservation.

However, computational fluid dynamics (CFD) is very complicated in dealing with the droplet-air interface, and solving the pressure filed and velocity field also need a lot of computational resources [22]. Recently, the lattice Boltzmann (LB) method has been widely applied to simulate the droplet impacting process, because LB method requires less computational resources and is easier to be implemented in parallel computing [23, 24]. Furthermore, the LB method can easily model the complicated boundary conditions in mesoscale and capture the characteristics at the droplet-air interface, therefore it has a natural advantage in dealing with mesoscale two-phase flow with complex geometry [24-28]. More specifically for multiphase flow, scholars have developed many numerical models, such as Shan-Chen model [29, 30], color-gradient model [31], free energy mode [32] and phase field model [33]. Therefore, based on these multiphase LB models, some research works have been reported to study the impacting process between droplet and solid obstacle. Gac and Gradon [34] numerically investigated drop impact on spherical obstacles via two-color LB method, and they observed that as We number gradually increasing, the droplets fused first, and then ripped, coated and formed many satellite droplets. Zhang *et al.* [35] studied the droplet spreading characteristics of droplet impact on spherical solid by using the three-dimension single relaxation time (SRT) LB method (LBM). However, SRT model could not precisely simulate the droplet collision process with low viscosity and large We number. In addition, the highest the density ratio (DR) of gas and liquid (DR= ρ_l / ρ_g , where the subscript g and l represent gas phase and liquid phase, respectively) was only 328 in their work. Recently, Raman *et al.* [36] studied the dynamics changes of the droplet when two droplets impacted the same and different positions of the solid successively. They mainly focused on the effects of the initial position of two droplets, the Ohnesorge number and the We number on droplet spreading process, and the result show that the wetting properties of the substrate had a great influence on the fusion of the droplets. However, the phase-field model coupled with the traditional CFD method was incorporated into the LB method, which significantly increased the requirements of computational resources by the LBM.

The pseudopotential multiphase model proposed by Shan and Chen [29, 30] has been widely applied in the multiphase flow in recent years because it does not require any explicit interface tracking technique and has much less computational load than other models [22, 37, 38]. Some scholars also used the Shan-Chen model to study the process of droplet impacting on solid. Li *et al.* [39] utilized the pseudopotential LB method to study the dynamic behaviors of droplet passing through long channel with circular obstacles under the gravitational force. Effects of the distance of spherical obstacle from the center of the droplet, the gas-liquid viscosity ratio, the wetting characteristic and the Bond number on the physical deformation and fragmentation were investigated. They found that the distance of the axis of solid obstacle from the centerline can achieve both the results of separation and non-separation of the droplet, therefore they concluded that as the wettability of the walls increasing, the droplet would fall from the top of the solid to the bottom of the solid. However, the DR was only maintained as 1.0. Furthermore, the Shan-Chen model has large spurious velocity, it cannot handle large DR and low viscosity flow, and it cannot adjust the surface tension independently [40]. Therefore, a lot of researchers tried to improve the Shan-Chen model by overcoming the aforementioned disadvantages. Mccracken and Abraham [41] applied the multi-relaxation-time (MRT) model to handle the low-viscosity flow. Benzi *et al.* [42] added a virtual density to achieve the wetting properties of the droplet on the wall. Li *et al.* [40] amended the external force terms in the MRT model to achieve thermodynamic consistency under large DR and independent adjustment of surface tension. Most recently, Li *et al.* [43] corrected the contact angle of Shan-Chen model. However, the spurious velocity was too large when the contact angle was very small or very large. Therefore, this paper coupled the Shan-Chen model with MRT collision model, high DR model, independent surface tension adjustment model and wall wetting characteristic.

In this paper, a series of verifications were performed such as thermodynamic consistency at large DR, Laplace's law, droplet impact onto the liquid film, surface tension adjustment, wetting and fusion properties of the walls. It was found that, under large DR, this model met the thermodynamic consistency well and can deal with two-phase flow with low viscosity, the spurious velocity was small when achieving small or large contact angle, at the same time it can tune surface tension while keeping the same DR. After reviewing of the previous literature on the numerical simulation of droplet impact on solid, it was found that most of literature were chosen to study the spherical solid obstacle, but to the authors' best knowledge, nobody ever considered the splitting liquid after impacting the solid obstacles and limited studies have been reported to particularly focus on square solid obstacles. Furthermore, the literature of droplet impact onto solid via LBM did not realized the large DR and large Reynolds (Re) number. Therefore, in this paper, the improved large DR pseudopotential MRT-LBM multiphase model was employed to study the droplet impacting square obstacle in detail. Effects of a wide range of Re number, We number, wetting characteristic of solid obstacle, ratio of obstacle size to droplet diameter (χ_1), ratio of channel width to droplet diameter (χ_2)on the deformation and breakup of droplet when impacting on a square obstacle were investigated..

2. Numerical model

In this section, an improved Shan-Chen model will be clearly discussed. Luo *et al.* [47] and McCrachen & Abraham [41] proposed a multi-relaxation-time (MRT) LB model to realize better numerical stability instead of the BGK model because its consider the high-order parameters in moment space compared the SRT model, where the collision distribute function(DF) can be given as [41, 48]:

$$f_\alpha(\boldsymbol{x}+\boldsymbol{e}_\alpha\delta_t,t+\delta_t)-f_\alpha(\boldsymbol{x},t)=-\overline{\Lambda}_{\alpha i}\left(f_i-f_i^{eq}\right)\Big|_{(\boldsymbol{x},t)}+\delta_t\left(S_\alpha-0.5\overline{\Lambda}_{\alpha\beta}S_\beta\right)\Big|_{(\boldsymbol{x},t)} \tag{1}$$

where f and f^{eq} represent the particle DF and the equilibrium DF respectively, δx and δt are the lattice space step and the time step, and both were set to be equal to 1, so $c=\delta x/\delta t=1$, e_a denotes the discrete velocity along the direction of a [49]. In this study, the D2Q9 model was adopted, so the discrete velocity can be given as:

$$\boldsymbol{e}_i=\begin{Bmatrix}(0,0), & i=0\\ (1,0)c,(0,1)c,(-1,0)c,(0,-1)c & i=1-4\\ (1,1)c,(-1,1)c,(-1,-1)c,(1,-1)c, & i=5-8\end{Bmatrix} \tag{2}$$

At the same time, $\overline{\boldsymbol{\Lambda}}=\boldsymbol{M}^{-1}\boldsymbol{\Lambda}\boldsymbol{M}$ is the collision matrix, $\boldsymbol{M}$ is the orthogonal transfer matrix, and $\boldsymbol{\Lambda}$ is the diagonal relaxation matrix in the moment space, which can be defined as [49]:

$$\begin{aligned}\boldsymbol{\Lambda}&=diag(s_0,s_1,s_2,s_3,s_4,s_5,s_6,s_7,s_8)\\&=diag(\tau_\rho^{-1},\tau_{\boldsymbol{e}}^{-1},\tau_\varsigma^{-1},\tau_j^{-1},\tau_q^{-1},\tau_j^{-1},\tau_q^{-1},\tau_\upsilon^{-1},\tau_\upsilon^{-1})\end{aligned} \tag{3}$$

where s is multiple-relaxation-time parameters, $s_1=s_2$, $s_3=s_5, s_7=s_8$, and the method how to choose those coefficients properly will be discussed in the next section. The non-dimensional relaxation time is defined:

$$\tau_\upsilon=\frac{1}{s_7}=\upsilon/c_s^{\,2}+0.5 \tag{4}$$

where υ is the kinematic viscosity of the fluid, and c_s is the lattice sound speed and is set to be $1/\sqrt{3}$.

As suggested in Ref. [50], the viscosity relaxation time is determined by:

$$\tau_v=\tau_g+\frac{\rho-\rho_g}{\rho_l-\rho_g}(\tau_l-\tau_g) \tag{5}$$

where subscripts g and l denote the gas phase and liquid phase respectively. By linear transformation, the DF f can be converted to the moment space $\boldsymbol{m}=\boldsymbol{M}\cdot f$, $\boldsymbol{m}^{eq}=\boldsymbol{M}\cdot f^{eq}$. The moment space DF $\boldsymbol{m}$ and the equilibrium DF $\boldsymbol{m}^{eq}$ are given by [47, 51]:

$$\underbrace{\begin{bmatrix}\boldsymbol{m}_0(\rho)\\ \boldsymbol{m}_1(e)\\ \boldsymbol{m}_2(\varepsilon)\\ \boldsymbol{m}_3(j_x)\\ \boldsymbol{m}_4(q_x)\\ \boldsymbol{m}_5(j_y)\\ \boldsymbol{m}_6(q_y)\\ \boldsymbol{m}_7(p_{xx})\\ \boldsymbol{m}_8(p_{xy})\end{bmatrix}}_{\boldsymbol{m}}=\underbrace{\begin{bmatrix}1&1&1&1&1&1&1&1&1\\ -4&-1&-1&-1&-1&2&2&2&2\\ 4&-2&-2&-2&-2&1&1&1&1\\ 0&1&0&-1&0&1&-1&-1&1\\ 0&-2&0&2&0&1&-1&-1&1\\ 0&0&1&0&-1&1&1&-1&-1\\ 0&0&-2&0&2&1&1&-1&-1\\ 0&1&-1&1&-1&0&0&0&0\\ 0&0&0&0&0&1&-1&1&-1\end{bmatrix}}_{\boldsymbol{M}}\underbrace{\begin{bmatrix}f_0\\ f_1\\ f_2\\ f_3\\ f_4\\ f_5\\ f_6\\ f_7\\ f_8\end{bmatrix}}_{f},\quad \boldsymbol{m}^{(eq)}=\begin{bmatrix}\rho\\ -2\rho+3(j_x^2+j_y^2)\\ \rho-3(j_x^2+j_y^2)\\ j_x\\ -j_x\\ j_y\\ -j_y\\ j_x^2-j_y^2\\ j_xj_y\end{bmatrix} \tag{6}$$

where j_x and j_y are equal to ρu_x, ρu_y respectively.

The evolution of the MRT-LB equation (1) consists two steps, i.e. the collision step and streaming step. The collision step is projected onto the moment space the moment space, while the streaming process is carried out in the velocity space.

With the aid of Eq. (3) and Eq. (6), the right-hand side of Eq. (1) can be expressed as [43]:

$$\boldsymbol{m}^{*} = \boldsymbol{m} - \Lambda(\boldsymbol{m} - \boldsymbol{m}^{eq}) + \delta_t(\boldsymbol{I} - \frac{\boldsymbol{\Lambda}}{2})\overline{\boldsymbol{S}} \tag{7}$$

where $\boldsymbol{I}$ is the unit tensor, $\overline{\boldsymbol{S}} = \boldsymbol{MS}$ is the forcing term in the moment space, and $\boldsymbol{S}=(S_0,S_1,S_2,S_3,S_4,S_5,S_6,S_7,S_8)^T$, and the streaming process can be expressed as [49]:

$$f_i(\boldsymbol{x} + \boldsymbol{e}_i\delta_t, t + \delta_t) = f_i^{*}(\boldsymbol{x}, t) \tag{8}$$

where $f^{*}=\boldsymbol{M}^{-1}\boldsymbol{m}^{*}$.

For the pseudopotential MRT LB model, the macroscopic density and velocity are determined by [44]:

$$\rho = \sum_i f_i, \quad \rho\boldsymbol{u} = \sum_i e_i f_i + \frac{\delta_t F}{2} \tag{9}$$

where $F = (F_x, F_y)$ is the total force acting on the pseudopotential MRT LB model. For the fluid-fluid interaction force in the Shan-Chen model for multiphase flow can be given by [40, 44]:

$$\boldsymbol{F}_m = -G\psi(\boldsymbol{x}, t)\left[\sum_i w(|\boldsymbol{e}_i|^2)\psi(\boldsymbol{x} + \boldsymbol{e}_i, t)\boldsymbol{e}_i\right] \tag{10}$$

where G is the interaction strength with a positive (negative) sign for a repulsive (attractive) force between particles, $w(|\boldsymbol{e}_a|^2)$ is the weight factor [44]. For the case of D2Q9 model, the weights are $w(1)$ =1/3 and $w(2)$ = 1/12. ψ represents the effective mass.

By overcoming the aforementioned drawbacks in the previous section, a modified forcing term proposed by Li *et al.* [49], which can be defined in the moment space as Eq.(11), was integrated with the MRT LB model in order to simulate flow with large DR (e.g., DR=1000).

$$\overline{\boldsymbol{S}} = \begin{bmatrix} 0 \\ 6(u_x F_x + u_y F_y) + \dfrac{12\theta|\boldsymbol{F}_m|^2}{\psi^2\delta_t(\tau_e - 0.5)} \\ -6(u_x F_x + u_y F_y) + \dfrac{12\theta|\boldsymbol{F}_m|^2}{\psi^2\delta_t(\tau_\varsigma - 0.5)} \\ F_x \\ -F_x \\ F_y \\ -F_y \\ 2(u_x F_x - u_y F_y) \\ (u_x F_y - u_y F_x) \end{bmatrix} \tag{11}$$

where θ is utilized to adjust the numerical stability in the proposed pseudopotential MRT LB model, and the value will be given in the next section, $|\boldsymbol{F}_m|^2 = (F_{mx}{}^2 + F_{my}{}^2)$.

In this paper, choosing a suitable EOS in the pseudopotential model is the key n. Historically, there are three popular

EOS models [52], such as van der Waals EOS, Red-lich-K Wong (R-K)EOS and Carnahan-Starling (C-S) EOS, which were used in the pseudopotential. In the current study, Carnahan-Starling (C-S) EOS model was adopted [46]:

$$P_{EOS} = \rho RT\frac{1+b\rho/4+(b\rho/4)^2-(b\rho/4)^3}{(1-b\rho/4)^3}-a\rho^2 \tag{12}$$

where $a=0.4963R^2T_c^2/p_c$, $b=0.18727RT_c/p_c$.

Therefore, the critical temperature is equal to $Tc=0.3773a/(bR)$, T_c and p_c are the critical temperature and pressure, respectively. In this study, b =4, R =1, c =1, δ_t=1, and ψ in Eq. (11) can be defined as [52]:

$$\psi=\sqrt{\frac{2(P_{EOS}-\rho c_s^2)}{Gc^2}} \tag{13}$$

Tuning surface tension is very difficult in the pseudopotential model. In early literature, it only can be realized by choosing different density ratios, which is greatly limited by the applications. Therefore, Sbragaglia *et al.* [53] proposed multi-range potential model to tune surface tension independently. However, using the multi-range potential model, the density ratio will vary with the surface tension accordingly [45]. Li *et al.* [40] modified the MRT pseudopotential model by adding an additional source term in the MRT-LB moment space and ensured that the DR did not change. The modified collision equation in the moment space can be given as:

$$\boldsymbol{m}^{*}=\boldsymbol{m}-\Lambda(\boldsymbol{m}-\boldsymbol{m}^{eq})+\delta_t(\boldsymbol{I}-\frac{\boldsymbol{\Lambda}}{2})\bar{\boldsymbol{S}}+\delta_t\boldsymbol{C} \tag{14}$$

where $\boldsymbol{C}$ is additional source term in the MRT-LB and defined as [40]:

$$\boldsymbol{C}=\begin{bmatrix}0\\ 1.5\tau_e^{-1}(Q_{xx}+Q_{yy})\\ -1.5\tau_\varsigma^{-1}(Q_{xx}+Q_{yy})\\ 0\\ 0\\ 0\\ 0\\ -\tau_\upsilon^{-1}(Q_{xx}-Q_{yy})\\ -\tau_\upsilon^{-1}Q_{xy}\end{bmatrix} \tag{15}$$

In Eq. (24) Q_{xx}, Q_{yy} and Q_{xy} can be calculated via the following equation [40]:

$$\boldsymbol{Q}=k\frac{G}{2}\psi(\boldsymbol{x},t)\left[\sum_{i=1}^{8}w(|\boldsymbol{e}_i|^2)[\psi(\boldsymbol{x}+\boldsymbol{e}_i,t)-\psi(\boldsymbol{x},t)]\boldsymbol{e}_i\boldsymbol{e}_i\right] \tag{16}$$

where $\boldsymbol{Q}=\left(Q_{xx},Q_{yy},Q_{xy}\right)$ is the discrete pressure tensor, k is the parameter that can precisely tune the surface tension in the proposed pseudopotential MRT LB model [40].

In this paper, because there is the three-phase contact line, therefore we need to consider the wall wetting characteristics. Benzil *et al.* [42] employed ghost density on the wall to mimic the interaction between the solid and the fluid. By adjusting the density of the solid, the method can achieve different wall wetting characteristic. However, Li *et al.* [43] found that the droplet above the solid is suspended in the gas when achieving the wall wetting characteristic.

Therefore, Li *et al.* further modified the solid-fluid pseudopotential force on the wall, and the equation is as follows [43]:

$$\boldsymbol{F}_{ads} = -Gw\psi(\boldsymbol{x},t)\left[\sum_i w(|\boldsymbol{e}_i|^2)\psi(\boldsymbol{x},t)s(\boldsymbol{x}+\boldsymbol{e}_i)\boldsymbol{e}_i\right] \tag{17}$$

where $s(x+e_i)$ is a switch function, which is equal to 0 and 1 for solid and fluid respectively, and Gw is the parameter to tune wetting ability of the solid wall [43] . Subsequently, the total force in the Eq. (9) and Eq. (11) is $\boldsymbol{F} = \boldsymbol{F}_m + \boldsymbol{F}_{ads}$.

3. Model verification

In this paper, the proposed pseudopotential MRT-LB model was verified by its thermodynamic consistency, Laplace's law, droplet impact onto a thin liquid film, surface tension tuning and droplet wetting wall respectively.

3.1. Thermal consistency

In order to verify the thermodynamic consistency of the proposed model, the Maxwell construction theory was utilized to compare with the results predicted by the MRT LB model. A horizontal liquid film with a thickness of 50 lattice units was placed in the middle of a grid size $Nx \times Ny = 200 \times 200$ square computational domain, the periodic boundary condition was employed, and the initial density field was defined as follows [45, 54]:

$$\rho = \rho_g + \frac{\rho_l - \rho_g}{2}\left[\tanh\left(\frac{2(y - y_1)}{W}\right) - \tanh\left(\frac{2(y - y_2)}{W}\right)\right] \tag{18}$$

where $W = 5$, y_2 and y_1 are the location of the gas-liquid interface and the thickness of the interface is 50 lattice units, so $y_2 = 125$ and $y_1 = 75$.

The Carnahan-Starling (C-S) EOS was adopted in this study, and the parameter a in Eq. (12) was set to be 0.25. For the parameter G in Eq. (8) was set to be -1, while G would be changed to -1/3 if T/T_c is less than 0.6. It was found that shortening the second order moment relaxation time in the MRT model can greatly improve the numerical stability. Therefore, in order to ensure the stability and convergence of this pseudopotential MRT LB model, the relaxation times in Eq. (3) were chosen as follows: $\tau_\rho = \tau_j = 1.0$, $\tau_e^{-1} = \tau_\varsigma^{-1} = 0.51$, $\tau_q^{-1} = 1.1$. The parameter θ in Eq. (11) was set to be 0.114, and the kinematic viscosity of liquid and gas were both set to be 0.1. The gas and liquid densities obtained from the Maxwell construction theory and the pseudopotential MRT LB model are listed in Table 1, and the comparison of three different density ratios from Ref. [49] is also included in Table 1. It can be concluded that the proposed pseudopotential MRT LB model can satisfy the thermodynamic consistency well even when the DR is high like 1000 when $T/T_c = 0.48$ from Table 1.

3.2. Laplace's law and spurious velocity

The verification of Laplace's law ($\Delta p = \sigma / R$, σ is surface tension, R is the radius of the droplet) is a classic case using LBM model. In this study, droplets with various radius were placed at the center of a $Nx \times Ny = 200 \times 200$ grid size domain, and periodic boundary conditions were employed. The multiple-relaxation-time coefficients and the kinematic viscosity of gas phase and liquid phase still kept the same as Section.3.1. The initial density field distribution can be defined

as [54]:

$$\rho(\mathrm{x,y})=\frac{\rho_l+\rho_g}{2}-\frac{\rho_l-\rho_g}{2}[\tanh(\frac{2(\sqrt{(x-x_0)^2+(y-y_0)^2})-R_0)}{W})] \tag{19}$$

where x_0, y_0 are the coordinates of centroid in the domain. Other parameters and conditions were maintained the same as Section 3.1.

Fig. 1 (a) and (b) present the density field distribution, spurious velocity vector, and spurious velocity contour for T/T_c = 0.48 corresponding to DR=1000, and the white line marked in Fig.1 (b) is the two-phase interface. One can observe from Fig.1 that the spurious velocity only appears in the gas phase and around the two-phase interface, while the spurious velocity of liquid phase is almost equal to 0. Fig. 2 demonstrates the density change versus x at the center of Y-axis and the relationship between the surface tension and gas-liquid kinematic viscosity ratio (KVR). From Fig. 2 the gas-liquid interface thickness is approximately 5~6 lattice units and the surface tension does not change with KVR when the DR is as high as 1000. The pressure difference between the inside and outside of the droplet with different radius is given in Fig.3 when T/T_c is equal to 0.48 and 0.6. It is very important that the pressure difference is linear with the reciprocal of droplet radius at different density ratios.

To investigate the spurious velocity with different densities, the stationary liquid droplet with different density ratios at different parameter values of a=0.25 and 0.5 in Eq. (12) was explored. The relationship between the maximum spurious velocity and DR at a=0.25 and 0.5 is demonstrated in Fig.4, where the maximum spurious velocity is equal to 0.0038 at a = 0.25 and T/T_c = 0.50, which is in a good agreement with the spurious velocity of 0.0039 in Ref. [49]. From the macroscopic point of view, the maximum spurious velocity increases with the increasing of DR. While the smaller the value of a is, the smaller the maximum spurious velocity is, and this effect is more evident for larger density ratios under the same DR. In summary, the maximum spurious velocity predicted by the proposed MRT LB model can be maintained around 10E-03 even if the DR is as high as 1000 when a=0.25.

3.3. Droplet splashing on a thin liquid film

In the improved pseudopotential MRT LB model, although the Laplace's law can be verified using stationary droplets, the evolution of gas-liquid interface is difficult to capture because of the large spurious velocity. Therefore, droplet splashing on a thin liquid film was utilized to verify the accuracy of this model to capture the two-phase interface under large DR, large We number and large Re number. A computational mesh of $Nx \times Ny$=600 × 200 was adopted in current study, and the diameter of the droplet was set as 80 lattice units. The liquid film was located in the bottom of the domain where its height was one fourth of the diameter of droplet, and the initial impact velocity was assumed as $(u_x, u_y) = (0, -U)$, where $U = 0.12$. The temperature ratio was set to be T/T_c = 0.50 corresponding to DR of 750 [49], and the non-slip boundary condition was employed in the y direction while the period boundary condition was used in the x direction. The gas kinematic viscosity was υ_g=0.0333, the liquid kinematic viscosity was set to be Case A: 0.06667 and Case B: 0.00667, respectively. Therefore, the Re number of Case A and B are 143.23, 1432.30, respectively. The surface tension was assumed as σ=0.0029, thus $We = \rho_l U^2 D/\sigma$ =180.63. Other parameters were kept the same as Section 3.2. The dimensionless time (DT) was defined as

$t^* = tU / D$, and t^* =0.0 was assumed as the moment when the droplet touches the thin liquid film.

The temporal evolution of the interface is showed in Fig.5 for Case A (Re =143.23) and Case B (Re =1432.30). It can be observed from Fig.5 that when the droplet collides on the thin liquid film, a crown wall is formed and widening as time is marching. Furthermore, when the Re number is increased by 10 times, the crown wall is splashed and two satellite droplets are formed eventually. Fig.6 shows the time evolution of the non-dimensional crown radius r / D of Case B versus DT, where the predicted spread factors agrees well with the experimental data of power law from Refs. [55, 56], which is $r / D = 1.29\sqrt{t^*}$.

3.4. Surface tension

To further verify the capability of the improved pseudopotential MRT LB model tuning the surface tension independently from the DR, following Ref. [40], the parameter k in Eq. (16) was chosen for verification using the Laplace's law and the droplet's impact onto a thin liquid film. The reduced temperature was set to be T / T_c = 0.50, The multiple-relaxation-time coefficients still kept the same as Sectoin.3.1, while the kinematic viscosity of gas phase and liquid phase were set to be 0.033 and 0.006667, respectively. Fig. 7 presents the relationship of pressure difference between inside and outside of the droplet versus $1/R$ for three cases: 1-k =1.0, 1-k =0.75 and 1-k =0.25. It can be seen that the surface tension gradually reduces with the increasing of the parameter k. Moreover, it is important to note that the pressure difference is still linear with the reciprocal of droplet radius at different values of 1-k.

At the same time, the simulation of a droplet impacting a liquid film was carried out by using different values of k. The gas and liquid kinematic viscosity were set to be 0.16666 and 0.066666, respectively. Other parameters and conditions were kept the same as Section 3.3. The density contour of liquid droplet and thin film, as well as their collision, can be found in Fig.8 for 1-k =1.0, 1-k =0.75 ,1-k =0.5 and 1-k =0.25 at t^* =2.64. As shown, with the same as DR, increasing k solely will cause the splash of crown wall and the appearance of satellite droplets.

3.5. Contact angle

In Ref. [43], the model proposed by Li can adjust the contact angle well after adding the pseudopotential force between the wall and the fluid. However, it was found that when the wall wettability was too strong or too weak, the spurious velocity was too large by considering the liquid-solid force. Therefore, in this paper, the boundary condition of the solid wall was changed to the halfway bounce-back scheme [57] without increasing the flow-solid force. In order to verify this proposed boundary conditions, we conducted a detailed verification by implementing the contact angle. We chose the grid calculation of the size of $Nx \times Ny$ =400 × 200 , and the initial droplet placed above the solid wall to observe the wetting characteristic. The droplet radius was set to be 50, meanwhile, the initial ordinate of the droplet was (Nx/2, 50). For DR and other parameters were the same as Section 3.4. Fig. 9 is given to show the wetting process at the same time where Gw equals to -0.2, 0.0, 0.2. From Fig. 9, one can observe that the droplet gradually spread along the wall with the passage of time. However, the liquid droplet wetting process differed at different Gw at the same time. The droplet wetting length increases with decreasing Gw.

In order to accurately investigate the spreading process of droplet along the different wetting characteristic (CA) walls.

The droplet wetting process changing over time when Gw equals to -0.2, -0.1, 0.0, 0.1, 0.2 can be found in Fig. 10. Fig.10 also presents the power law ($R \propto t^n$) [6] fitting for five different spreading processes. It can be demonstrated that the wetting characteristic of the droplet is in good agreement with Power law [6]. Furthermore, increasing the wetting ability of the wall, the exponent parameter of n in the power law will be increased, which is in good agreement with experimental data and the numerical simulation results of molecular dynamics [58, 59].

Fig.11 also shows the stable state of the droplet along the wall at different Gw, and we find that different Gw can achieve the adjustment of wetting characteristic of the wall. Fig.12 shows the relationship between contact angle and Gw, which is almost linear correlation. Fig.13 indicates that when the Gw equals to -0.1, 0.0, 0.1, the two-phase velocity vector diagram of the stabilized droplet can be seen from the figure. The large velocity vector only appears at the interface. In order to verify the magnitude of the spurious velocity at different Gw, Fig.14 presents the spurious velocity of different wall wetting characteristics as a relaxation time equals to 0.8 . It can be seen that even at CA=27°, the spurious velocity is still less than 0.03 which is much smaller than the data in Fig.9 in Ref. [43].

To sum up, after using the new wall boundary condition and the pseudopotential force on the wall, it can be guaranteed that Gw has the ability to adjust the wetting characteristics of the wall and with less spurious velocity even if the DR reaches 750.

4. Results and discuss

Fig.15 illustrates the initial state of the droplet impact on the solid particles in the microchannel. In this figure, the droplet and the solid particle are located on the center line of X-axis, where the droplet diameter is D and the length of the square solid particles is a. It was defined that at the initial collision time, the initial velocity of the droplet was set as $(u_x, u_y)=(0,\mathrm{U})$. At the same time, the shortest distance between the droplets and the solid particles in the Y- axis direction was defined as h. In addition, the rest of the domain is gas-phase region. In this simulation, the boundary conditions of no-slip wall were set in the left and right wall, the periodic boundary conditions were employed in the upper and lower wall, and the non-slip wall boundary conditions were still adopted for the solid particles in the computational domain. The new DT was defined as $T = Ut / D$, and assuming $T = 0$ as the time of the droplet starting falling. In order to better describe the process of droplet impact on solid particles at different parameters, we defined characteristic parameter: Re number and We number. And they can be expressed as:

$$Re = \frac{UD}{\upsilon} \tag{20}$$

$$We = \frac{\rho U^2 D}{\sigma} \tag{21}$$

where U is the initial velocity of the droplet, D represents the diameter of the droplet, υ denotes the kinematic viscosity of the droplet, ρ and σ are the density and surface tension of the droplet.

In order to discuss the effect of solid particle size on the droplet impacting process, the ratio of the solid obstacle length and the droplet diameter was defined as follows:

$$\chi_1 = \frac{a}{D} \tag{22}$$

To find the effect of the width of the channel on the droplet impacting process, we defined the ratio of the channel width and the droplet diameter as Eq. (23).

$$\chi_2 = \frac{Nx}{D} \tag{23}$$

where Nx is the width of the channel.

The following dimensionless length was also defined to describe how the distance from the solid obstacle can affect the impacting process:

$$\chi_3 = \frac{\mathrm{h}}{D} \tag{24}$$

It is worth noting that the lattice unit was adopted for all the dimensionless lengths in the computational process in this paper.

The relaxation times for the pseudopotential MRT-LB model were selected the same as Section 3.1. The reduced temperature was chosen as T/Tc=0.50 corresponding DR= 750, and without specified description, the gas-liquid density ratio kept constant. Next, it will discuss the effects of Re number, We number, gas-liquid kinematic viscosity ratio (KVR= υ_g / υ_l), gas-liquid density ratio (DR = ρ_l / ρ_g), the geometry dimensionless parameter and the shape of solid partial. In order to clearly describe the process of the droplet stretching and rupturing over time, the maximum interface width of the droplet along the horizontal and vertical directions as H , L was defined as shown in Fig.16. And the horizontal and vertical dimensionless lengths can be defined as follows:

$$\zeta_1 = \frac{\mathrm{L}}{D} \tag{25}$$

$$\zeta_2 = \frac{\mathrm{H}}{D} \tag{26}$$

4.1. Effects of Reynolds number

A computational domain was chosen as $Nx \times Ny$=300 × 500 lattice units. As suggested in Ref. [60], the radius of droplet should be large than 60 lattice units, therefore in this study the diameter of the droplet was set as D =100 lattice units, and the center coordinates of the droplet were Nx /2 in the horizontal direction and 350 in the vertical direction respectively. In this part, the length of the square particle located at the bottom of the droplet was set as 40 lattice units and the shortest distance of the droplet to the square solid was 80 lattice units, so the dimensionless parameter χ_3 was equal to 0.8. Without specified description, χ_3 was kept as constant in the following sections. The initial velocity of the droplet was set as U =0.02 and correspondent Re number was Re =300. Because the MRT collision model was chosen in this paper, which allowed us to deal with the low viscosity fluid flow. In this section, the kinematic viscosity of gas and liquid were set to be 0.1, 0.006667, respectively, and DR was 750. Therefore, the values of DR and KVR were close to the ratio of the water to air (DR=773, KVR=15). Besides, contact angle was set as 90°, namely, Gw =0.0.

Fig.17 shows the dependence of interface evolution over time during the droplet impacting solid particle at Re =300, DR=750, KVR=15. In this figure, ΔT was set as 0.08 in each frame of Fig.17, and the first frame image of the DT is T =0.08. (Without specified description, the initial moment and time step are consistent in the remaining sections). We can see

that the droplet gradually move toward the solid at a given initial velocity (See $T = \Delta T$, $2\Delta T$, $3\Delta T$) as show in Fig.17; at T = $4\Delta T$, we find that the droplet lean on the upper wall of the square obstacle and then continue to fall along the solid wall under the effect of the inertial force of the droplet (See T =$5\Delta T$, $6\Delta T$, $7\Delta T$). Then the droplet continues to fall along the wall surface, and finally wraps the square solid particle.

In order to investigate the effect of the initial Re number on the droplet colliding solid particles, we increase the Re number to 750. The evolution of the interface over time is given by Fig.18. From the figure, one can observe that as the initial droplet Re number increasing, the rate of expansion of the droplet accelerates towards to the both sides of the solid particle at T =$3\Delta T$. Besides, the droplet falls along the wall further as time goes on. However, compared with the situation of Re =300, the wetting distance is much longer downwards. At T =$5\Delta T$, the height of droplet interface surpasses the height of the bottom of the solid. Under the inertial force, the droplet further falls. Finally, the droplet is separated into two small secondary droplets due to the solid obstacle, but the drop does not breakup still at T =$12\Delta T$.

We further increased the Re number to 1200. Fig.19 presents the evolution of the two-phase interface over time at the same time step. It can be seen that at $T = \Delta T$, the droplet completely wetted the upper wall, and then the droplet does not move along the wall as shown in Fig.19. On the contrary, the droplet expands towards both sides of the solid (See T =2 ΔT). However, at $T = 3\Delta T$, the droplet still wets the left wall and right wall, which may be due to the large shear stress on the droplet at the vertical boundary of the solid obstacle and the droplet rupture under inertial force. At the same time, the droplet continues to stretch in two sides of the solid particle (See T =$6\Delta T$, $7\Delta T$, $8\Delta T$). Furthermore, we observe that the spherical droplet on the left and right sides of the solid gradually is stretched and then it forms long ligaments (See T =9 ΔT , $10\Delta T$), and we also find that the droplet is split into three parts. In the subsequent stretching process, the two layers of liquid film on the left and right walls of the solid start to separate from the solid (See T =$11\Delta T$); finally, the liquid film stretched downwards is further fragmented and broken by the surface tension and two satellite droplet are formed (See T =$12\Delta T$), but the droplet above the solid remains on top of it without changing its shape.

In summary, it can been seen that the results of a droplet impacting on solid is that at a small Re number, the droplet slowly wets the wall, and when Re further increases, the droplet along the solid obstacle falls faster, but does not form a thin liquid film. After the Re number increases to 1200, the droplet spreads to the both sides of the solid rapidly after the droplet collision, and then form a long and thin liquid film, and the droplet is separated into satellite droplets finally. Therefore, it is demonstrated from the three Cases that increasing the Re number of droplet will cause more intense dynamic behavior.

4.2. Effects of Weber number

It has no doubt that the We number is the key characteristic parameter to control the dynamic performance of droplet impacting on solid obstacles. Therefore, in this section, we explored the effect of We number on dynamic behavior of droplet colliding solid particle. Due to the limitation of LB model itself, it is extremely difficult for tuning surface tension independently on droplet colliding solid obstacles in prior literature. However, the improved pseudopotential LB model with addition force term, which makes us tune surface tension easily. In the computational setting, the DR, computational domain and other conditions still keep the same as Section 4.1, which means the DR is 750 and KVR is 15, and the Re number of all the cases still is equal to 1200. However, the different surface tension of the droplet can be realized the parameter of k in

the Eq. (16). The different parameter k were chosen as Case a: k =-0.5, Case b: k =0.0 and Case c: k =0.5, respectively. As a result, the surface tension obtained by the Laplace's law were Case a: σ=0.0065, Case b: σ=0.0042, and Case c: σ =0.002 respectively. Fig. 20 illustrates the multiphase interface evolution at the same DT corresponding Case a, Case b, Case c, respectively.

Notice the picture that, at the beginning of the droplet colliding solid particle, three is no differences in the interface evolution(See $T = \Delta T$, $2\Delta T$); but at the next moment, we find that with the increase of We number, the two layers of liquid film become longer and thinner along the both sides of the solid. At the same time, While keeping Re number constant, the smaller We number is, the larger surface tension of the droplet is, and the drop wetting rate becomes faster(See $T = 3\Delta T$). Then we observe that the liquid film connecting the left and right sides of the solid becomes longer and thinner in Case a but the size of the droplet at the end is larger(See $T = 4\Delta T$). Moreover, at large radius of curvature, the first rupture of the film occurs in Case a and it does not take place at the same time for Case b and Case C (See $T = 5\Delta T$). Finally, the liquid film becomes more and more slender under pull force and breaks up for Case c. And the droplet formed due to the rupture of the film adheres to the top of the solid particle while the secondary satellite droplets formed by Case a and Case b remain in the gas phase. However, it can be found that the satellite droplet on the top wall have no difference in three cases.

In order to quantify the outcome of droplet impacting on solid obstacle, we still track the dimensionless expansion length. The dimensionless expansion length of Case a, Case b and Case c versus DT is given by Fig.21. From the figure we can observe that there is no change in the length of expansion of the drop along the left and right sides of the solid in the early stages of the collision, but increasing the We number will lead to longer expansion length, and this intends will be more obvious in the next time.

4.3. Effects of contact angle

The wetting property of the wall is a key parameter for the droplet striking the solid obstacle [61]. Although some scholars had carried out experimental studies on the droplet impact under different wetting walls [16] , but only three different wetting wall conditions were studied. At the same time, it is hard to get a lot of different wetting surfaces at one time without changing the geometric shape, but numerical simulation naturally has the convenience. Li et.al [39] numerically explored the dynamics of droplet past different wetting solid circular cylinder under gravity by LB method, but the velocity of droplet before contact with solid obstacle was very small. At the same time, the authors only focused on the movement of the droplet under the hydrophilic wall. Therefore, in order to full understand the influence of different wetting characteristics on the kinetic characteristics of droplet impacting on a solid obstacle, in this part, the contact angle was selected from hydrophilic to hydrophobic, and the CA was chosen as CA = 69.01 °, 90 °, 107.68 °, 123.14 °, 140.80 °. However, the other parameters remained unchanged, and it is guaranteed that DR=750, KVR=15, Re =1200, We =69.21.

In order to simplify the results, Fig.22 illustrates the time evolution of the two-phase interface over time at CA = 69.01 °, CA = 107.68 ° and CA = 140.80 ° at the same time, which corresponds with Case a, Case b and Case c in current study. It can be seen that at $T = \Delta T$, there is no difference between the three wetting walls, but at the next moment (T =2 ΔT) , we find that the droplet of Case a has wetted the wall, whereas Case b and Case c only expand to the left and right

sides; then (T =3 ΔT) the droplet in Case b begins to wet the wall, while the droplet has completely wetted the left and right walls in Case a. Further (T =4 ΔT), the liquid film in Case a has wetted the bottom of the solid while Case b and Case c still stretched only to the left and right sides. At T =5 ΔT , the droplet of Case a completely wets the whole solid while the bottom liquid film is further separated into two parts. At the same moment, the liquid films on both the left and right of Case b and Case C rupture. At the end (See T =6 ΔT), the liquid film at both sides of Case b is further split into two droplets, and impact on the left and right channel walls. Meanwhile, the liquid film in Case c has also impacted the left and right channel walls, but the front of the liquid film is slightly away from the wall. For Case b and Case c, there is a little difference that secondary droplets form on the top of the solid due to left-right liquid film rupturing. For the secondary droplet with CA = 107.68 °, the droplet still remains on the top wall of solid, whereas for CA = 140.80 ° the droplet has bounced up and stayed in the air. The reason is that wall wetting behavior in Case c is worse than one in Case b.

Fig.23 illustrates the relationship between the dimensionless length stretched of the liquid drop along the horizontal wetted wall and the DT. From the Fig.23, one can see that with the exception of CA = 90 °, as the wettability of the wall is weakened (CA $\rightarrow$ 180 °), the expansion length of the drop increases at the same moment. We also observe that the more hydrophobic the solid obstacle is, the shorter the time it takes for the liquid film to touch the channel wall. Further, Fig.24 shows the relationship between the dimensionless length in the vertical direction and the DT. It can be seen from the figure, in the case of different solid wetting wall, the stretched length of the droplet in the vertical direction changes a little. Or rather, it almost keeps constant.

4.4. Effects of solid particle size

In the case of keeping the diameter of the droplet equaling to 100, let the length of the square particle equaled to 20, 40, 60, 80. In this section, we still kept the same DR=750, KVR=15, and the computation domain $Nx \times Ny = 500 \times 300$ was employed. However, the Re number was set to be 900, and the contact angle was equal to CA=90°.

The snapshots of two-phase fluids after the droplet hits the solid at the same time when the solid side length to droplet diameter ratio is equal to χ_1=20/100, χ_1=40/100, χ_1=60/100, which corresponds to Case a, Case b and Case C, respectively is given by Fig. 25 . From the figure we can see that the smaller the solid particles, the faster the velocity of the liquid droplet wetting wall (See T =2 ΔT ,3 ΔT); from T =5 ΔT , the droplet has ruptured in Case a, however, the drops of Case b and Case c are still adhered to the wall. Finally, at T =6 ΔT , the droplet in Case a has completely dropped. The liquid film has also been split into two sections in Case b, whereas the Case c liquid film remains unbroken. We will divert attention to the droplet hanging on the solid particles. It can be concluded from the results that the size of the solid particle has a great influence on the droplet staying above the solid, and the size of the droplet left on the solid top increases with increasing χ_1.

In order to further investigate the effect of solid particle of different sizes on the droplet impacting and spreading process, Figs.26 and 27 show the relationship between the horizontal stretched length of the droplet and DT and the relationship between the vertical stretched length of the droplet and DT after the droplet impacts the solid particles of different sizes. From Fig.26, it can be seen that the size of the solid particle has a great influence on the interface change of the drop impact. When χ_1>0.5, the stretched length of the droplet at the same time is much larger than χ_1<0.5, but the change of the spreading length of the droplet is not obvious when increasing the size of solid particle. For χ_1<0.5, the stretched length in χ_1=0.4 is larger than one in χ_1=0.2 in the early stage of collision, but smaller in the late stage. As can

be seen from Fig.27, with the solid particle size remaining constant, the droplet dropping velocity is faster at the same time with the decrease of χ_1, and the stretching length is nearly linear with respect to the DT. On the other hand, the stretched length along the vertical direction increases with increasing the size of solid particle, and the stretched length is almost inversely proportional to the particle size.

4.5. Effects of channel width

In previous literature, droplet impacting solid particles occurs mostly in free space, therefore droplet impact in the microchannel is rarely studied, especially the effect of the width of the microchannel on droplet impact. Therefore, in this section, we studied the influence of the channel width to droplet diameter ratio on impacting process, and it should be noted that the dimeter of droplet and the length of square solid particle remained unchanged in different cases, and were set to be 100 lattice units and 40 lattice units, respectively. The ratios of the width of channel to droplet size were set as χ_2=150/100, χ_2=200/100, χ_2=250/100, χ_2=300/100, χ_2=350/100, χ_2=400/100, respectively. The DR, KVR, initial Re number of the droplet and We number were consistent with ones in Section 4.3. Liquid droplet and solid particle were placed in the center position of X-axis of the channel, and to ensure that χ_2=80/100. In the following, we will investigate the effects of different microchannel widths independently for the situation that without considering wetting characteristics, considering the hydrophilic wall and considering hydrophobic wall.

4.5.1. Without considering the wetting property of the wall

Fig.28 shows the interface evolution at the same moment in the process of a droplet colliding on a solid barrier without considering wetting property of the left and right wall of the channel corresponding to Case a: χ_2=150/10, Case b: χ_2 =250/100, Case c: χ_2=350/100. From the figure we can observe that at $T=\Delta T$, $2\Delta T$ there is no difference of the interfaces change under the three schemes; however, when T =3ΔT, the droplet has hit the channel wall in Case a, the droplet is still being stretched towards both sides in Case b and Case c. Then after T =5ΔT, the droplet has hit the wall in the Case b and the droplet continues to stretch in Case c. At the next moment, the droplet of Case a is split into a long liquid film and continues to fall under the inertial force and the counterforce of the wall of the droplet (See T =6ΔT). Finally, at T =8ΔT, se observe that in Case a, due to narrow channel widths and a larger area of the top liquid film continues to drop with its elongated liquid film. The falling liquid film in Case b has formed two satellite droplets while touching droplets on the wall to form folds, whereas the droplet in Case c freely develops towards both sides due to the wide channel length, but due to the surface tension and the inertia force, the elongated liquid film at both sides is again separated into an elongated liquid film, and finally the liquid droplet is divided into three secondary droplets and four liquid films.

Figs.29 and 30 indicate the evolution of dimensionless spreading length over time along the horizontal and vertical direction with different channel widths for droplet impacting on a square solid obstacle respectively. From Fig.29 we observe that as the width of the channel increasing, the deformation of the droplet first reaches the maximum when touching the wall and then bounces back and finally decreases gradually. At the same time, we also find that when χ_2<350/100, at the moment, the maximum spreading length reached before touching the wall is the same. When χ_2=350/100, the horizontal spreading process of the droplet will not be affected by the wall of the both sides.

It can be seen from Fig.30 that when T <1.5, at the same moment the vertical stretched length of the droplet with χ_2 =1.5 has the largest value, and the stretched length is almost the same under other parameters. However, the smaller the channel width, the larger the vertical stretched length of the droplet at the same time subsequently, which is due to the smaller the channel width, the earlier the droplet impinges on the wall, resulting in no horizontal development of the droplet.

4.5.2. Droplet impacting the hydrophilic solid particles in the walls of hydrophilic channel

Furthermore, we set the left and right walls as well as the solid particle to be hydrophilic, with CA = 69.01° and the other dimensionless parameters was consistent with Section 4.5.1. Fig.31 presents that process of the droplet impacting the solid particle when the channel width to droplet diameter ratios are χ_2=150/100, χ_2=250/100, χ_2=350/100 respectively at the same time. We find that there is no difference in the droplet interface deformation between the three schemes (See T = ΔT , 2 ΔT) at the beginning of the collision. However, at T =3 ΔT , droplet in Case a has hit the wall, while the droplet in Case b and Case c continue to stretch freely. At the next time (T =4 ΔT), the liquid film in the larger inertial force moves upwards, the droplet is still free to spread in Case b and Case c at this time. Lastly (see T = 6 Δ T) , due to the narrow channel in Case a, the liquid film has already wetted a very large part of the wall at high impact force, whereas the liquid film has just begun to wet the wall in Case b and the liquid film is still developing freely in Case c.

In the meantime, Fig.32 shows the evolution of maximum dimensionless length of the horizontal liquid film over the DT after the droplet collides with solid particle at the χ_2 ranging from 150 to 400. We find that the horizontal spreading of the droplet develops along droplet spreading process of the maximum microchannel. And only when the channel width is narrower and the interfacial width of the droplet reaches the maximum in the early period and will not change over time. This is because when the wall is a hydrophilic wall, the droplet contacts the left and right walls and will stick to the wall all the time, which leaves the width of the horizontal interface unchanged.

4.5.3. Drop impacting hydrophobic solid particle under the hydrophobic channel

The contact angle was set to CA=123.14°. Fig.33 presents the process of the droplet impacting solid particle under the condition that channel width to droplet diameter ratios are χ_2=150/100, χ_2=250/100, χ_2=350/100 respectively at the same time. It can be obtained from the instantaneous change in the interface that at $T = \Delta T$, hydrophilic and hydrophobic interfaces changing have no difference, but at T =2 ΔT , the droplet has hit the wall in Case A, the wetting phenomenon does not occur for the left and right sides of the solid particles. At the next moment (See T =3 ΔT), the liquid film does not wet the wall upwards like the hydrophilic wall when the liquid film touches the wall in Case a, but wets downwards. At the same time, because the wall is hydrophobic, the front of the liquid film is slightly away from the wall (See T =4 ΔT). Further (See T =5 ΔT), the liquid film at both sides ruptures, but the wider the channel width compared to Case a and Case b , the thinner the liquid film is stretched. Finally (See T =6 ΔT), the droplet above the solid of three schemes have become elliptical and substantially the shapes are the same, however, the liquid film has suffered different results at the bottom of the solid. Specially for Case c, the liquid film is further broken into two parts under joint action of the wall counterforce, surface tension and inertial force, however the liquid films are still stuck together in near the wall for Case a and Case b.

Furthermore, Figs.34 and 35 show that the evolution process of horizontal spreading dimensionless length and vertical

spreading dimensionless length over DT during the droplet impacting solid obstacle at different channel widths. From Fig.34, we can see that the processes of droplet impacting on the hydrophobic wall surface and the hydrophilic wall surface horizontal spreading are basically the same. This is because the droplet spreading process is greatly affected by the horizontal channel width. When decreasing the width of the channel, the droplet first contacts the wall surface, and the change is not made in the future. From Fig.35, one can observe that channel width has a little effect on the dimensionless vertical length, curves almost overlap together, but when the droplet hits the vertical walls, the dimensionless vertical length suddenly increases. Further, it can be concluded that after the drop collides with the solid wall, the vertical stretched length of the liquid film immediately approaches the vertical stretched length of the liquid film at the minimum channel width.

5. Conclusions

In this paper, a large DR pseudopotential MRT-LB model was developed. In this model, we added the external force term in the collision term to satisfy the independent regulation of surface tension. Furthermore, we also added the improved pseudopotential wall force to achieve the different wetting properties of the wall. In order to verify the accuracy of the model and the program, we validated the improved model by Laplace's law of stationary droplet in gas phase, calculation of spurious velocity under different DR, the spreading radius of the droplet impacting on liquid film and droplet wetting different wetting walls at large DR. It can be demonstrated that the model can satisfy thermodynamic consistency, can accurately capture the process of the droplet impacting the liquid film under large Re number, and We number, and agree with the experimental data [55, 56] and the process of the droplet spreading meets power law under different wetting walls [58, 59]. Finally, we applied the improved model to the droplet impacting on square solid obstacle. Effects of Re number, We number, the wall surface wetting properties, the size of solid particle and width of the microchannel on the deformation and rupture mechanism of the droplet were investigated, and the following conclusions can be expressed as:

a) At smaller Re number, the droplet glides directly along the solid obstacle without rupturing; further increasing the Re number, the shape of the droplet changes more during impacting and will form two independent droplets at both sides of the solid obstacle; with the further increase of Re number, the droplet spread quickly to the both sides of the solid after encountering obstacles, then the liquid film at both sides is stretched and form a small liquid film, and finally the liquid film splits into smaller droplet and liquid film under joint action of the inertia force and surface tension.

b) During the impacting process, the larger the We number, the more difficult it is for the droplet to maintain its initial state, which results in a more elongated liquid film on both sides of the solid particle, and at the same time, the liquid film expands toward both sides more quickly.

c) On the hydrophilic wall, the droplet in the process of impacting first wets the wall early, and the droplet ruptures under the solid obstacle accompanied by a layer of liquid film adhered to the solid obstacles as time goes on. For the hydrophobic wall, the more hydrophobic the walls, the faster the spread of the droplet to both sides. As the hydrophobicity of the wall becomes stronger, the droplet that is split above the solid instead bounces back, whereas the liquid film on the left and right sides is less susceptible for secondary breakup.

d) The smaller the square solid obstacle, the earlier the droplet ruptures, and the larger the size of the droplet forms at both sides. Further, we find that when χ_1 ranges from 0 to 1 , when χ_1>0.5 , the droplet spreads more rapidly to both sides, and when χ_1<0.5, the spread velocity of the drop to both sides greatly reduces. For the vertical spreading process, the

length of droplet spreading downwards for small solid particle is almost linear with the DT, and inversely proportional to the solid particle size.

e) The smaller the width ratio of the width of microchannel to droplet diameter, the more rapid droplet drops; at the same time, we find that when $\chi_2 > 300$, the height of the liquid film will be free to develop. For the hydrophilic wall, during the droplet impacting the left and right walls, some of the liquid film will spread upwards under the action of large inertia force, but the spreading velocity downwards is much greater than the spreading velocity upwards. For the hydrophobic wall, the liquid film at great velocity will still touch the wall but for smaller χ_2, and it is different from hydrophilic wall that the liquid film will not wet the wall upwards and only wet the wall downwards; at the same time, the front of the liquid film wetting the wall downwards will be slightly away from the solid wall.

Acknowledge

This work was supported by National Natural Science Foundation of China (No. 11562011, No. 51566012), Graduate Innovation Special Foundation of Jiangxi Province (No. YC2017-S056) and Jiangxi Provincial Department of Science and Technology (No. 2009BGA01800). The authors are also grateful for the support from New Faculty Support program at The University of Texas Rio Grande Valley. Special thanks are also due to Prof. Qing. Li from Central South University for his great help and valuable discussions on the theory and programing of this model.

Reference

[1] M. Wörner, Numerical modeling of multiphase flows in microfluidics and micro process engineering: a review of methods and applications, Microfluidics & Nanofluidics, 12 (2012) 841-886.

[2] J. Zhang, Lattice Boltzmann method for microfluidics: models and applications, Microfluidics & Nanofluidics, 10 (2011) 1-28.

[3] J. Wu, J.J. Huang, W.W. Yan, Lattice Boltzmann investigation of droplets impact behaviors onto a solid substrate, Colloids & Surfaces A Physicochemical & Engineering Aspects, 484 (2015) 318-328.

[4] P.R. Gunjal, V.V. Ranade, R.V. Chaudhari, Dynamics of drop impact on solid surface: Experiments and VOF simulations, Aiche Journal, 51 (2005) 59–78.

[5] H.K. Huh, S. Jung, K.W. Seo, J.L. Sang, Role of polymer concentration and molecular weight on the rebounding behaviors of polymer solution droplet impacting on hydrophobic surfaces, Microfluidics & Nanofluidics, 18 (2015) 1221-1232.

[6] P. Julien, A. Arnaud, Drop impact on a solid surface: short-time self-similarity, Journal of Fluid Mechanics, 795 (2015) 96-135.

[7] S. Mitra, M.J. Sathe, E. Doroodchi, R. Utikar, M.K. Shah, V. Pareek, J.B. Joshi, G.M. Evans, Droplet impact dynamics on a spherical particle, Chemical Engineering Science, 100 (2013) 105-119.

[8] Y. Zhu, H.R. Liu, K. Mu, P. Gao, H. Ding, X.Y. Lu, Dynamics of drop impact onto a solid sphere: spreading and retraction, Journal of Fluid Mechanics, 824 (2017).

[9] G. Liang, Y. Guo, Y. Yang, N. Zhen, S. Shen, Spreading and splashing during a single drop impact on an inclined wetted surface, Acta Mechanica, 224 (2013) 2993-3004.

[10] W. Choi, S. Leclear, J. Leclear, Abhijeet, K.C. Park, Drop impact on inclined superhydrophobic surfaces, Journal of Colloid & Interface Science, 461 (2016) 114-121.

[11] S. Bakshi, I.V. Roisman, C. Tropea, Investigations on the impact of a drop onto a small spherical target, Physics of Fluids, 19 (2007) 61-69.
[12] M. Pasandideh-Fard, M. Bussmann, S. Chandra, J. Mostaghimi, SIMULATING DROPLET IMPACT ON A SUBSTRATE OF ARBITRARY SHAPE, Atomization & Sprays, 11 (2001) 397-414.
[13] X. Liu, Y. Zhao, S. Chen, S. Shen, X. Zhao, Numerical research on the dynamic characteristics of a droplet impacting a hydrophobic tube, Physics of Fluids, 29 (2017) 180.
[14] G. Liang, Y. Guo, Y. Yang, S. Shen, Liquid sheet behaviors during a drop impact on wetted cylindrical surfaces ☆, International Communications in Heat & Mass Transfer, 54 (2014) 67-74.
[15] C. Josserand, S.T. Thoroddsen, Drop Impact on a Solid Surface, Annual Review of Fluid Mechanics, 48 (2017) págs. 365-391.
[16] S.A. Banitabaei, A. Amirfazli, Droplet impact onto a solid sphere: Effect of wettability and impact velocity, Physics of Fluids, 29 (2017) 419-441.
[17] C.S. Stevens, A. Latka, S.R. Nagel, Comparison of splashing in high- and low-viscosity liquids, Physical Review E Statistical Nonlinear & Soft Matter Physics, 89 (2014) 063006.
[18] C. Antonini, A. Amirfazli, M. Marengo, Drop impact and wettability: From hydrophilic to superhydrophobic surfaces, Physics of Fluids, 24 (2012) 673-687.
[19] A. Khayyer, H. Gotoh, Enhancement of performance and stability of MPS mesh-free particle method for multiphase flows characterized by high density ratios, Journal of Computational Physics, 242 (2013) 211-233.
[20] C. Josserand, L. Lemoyne, R. Troeger, S. Zaleski, Droplet impact on a dry surface: triggering the splash with a small obstacle, Journal of Fluid Mechanics, 524 (2005) 47-56.
[21] H. Gotoh, A. Khayyer, On the state-of-the-art of particle methods for coastal and ocean engineering, (2018) 1-25.
[22] L. Chen, Q. Kang, Y. Mu, Y.L. He, W.Q. Tao, A critical review of the pseudopotential multiphase lattice Boltzmann model: Methods and applications, International Journal of Heat & Mass Transfer, 76 (2014) 210-236.
[23] U. Frisch, B. Hasslacher, Y. Pomeau, Lattice-Gas Automata for the Navier-Stokes Equation, in: Phys Rev Let 56:1505-1508G Ilachinski, A, 1986, pp. 1505-1508.
[24] S. Chen, G.D. Doolen, LATTICE BOLTZMANN METHOD FOR FLUID FLOWS, Annual Review of Fluid Mechanics, 30 (2012) 329-364.
[25] J. Harting, C. Kunert, J. Hyväluoma, Lattice Boltzmann simulations in microfluidics: probing the no-slip boundary condition in hydrophobic, rough, and surface nanobubble laden microchannels, Microfluidics & Nanofluidics, 8 (2010) 1.
[26] Q. Li, Y.L. He, G.H. Tang, W.Q. Tao, Lattice Boltzmann modeling of microchannel flows in the transition flow regime, Microfluidics & Nanofluidics, 10 (2011) 607-618.
[27] S. Succi, E. Foti, F. Higuera, Three-dimensional flows in complex geometries with the lattice Boltzmann method, Epl, 10 (2007) 433.
[28] H. Huang, M.C. Sukop, X.Y. Lu, Multiphase Lattice Boltzmann Methods: Theory and Application, (2015) 1-17.
[29] X. Shan, H. Chen, Simulation of nonideal gases and liquid-gas phase transitions by the lattice Boltzmann equation, Phys Rev E Stat Phys Plasmas Fluids Relat Interdiscip Topics, 49 (1994) 2941-2948.
[30] X. Shan, H. Chen, Lattice Boltzmann model for simulating flows with multiple phases and components, Phys Rev E Stat Phys Plasmas Fluids Relat Interdiscip Topics, 47 (1993) 1815-1819.
[31] A.K. Gunstensen, D.H. Rothman, S. Zaleski, G. Zanetti, Lattice Boltzmann model of immiscible fluids, Physical Review A Atomic Molecular & Optical Physics, 43 (1991) 4320.

[32] M.R. Swift, E. Orlandini, W.R. Osborn, J.M. Yeomans, Lattice Boltzmann simulations of liquid-gas and binary fluid systems, Physical Review E Statistical Physics Plasmas Fluids & Related Interdisciplinary Topics, 54 (1996) 5041.
[33] X. He, X. Shan, G.D. Doolen, Discrete Boltzmann equation model for nonideal gases, Phys.rev.e, 57 (1998) R13-R16.
[34] J.M. Gac, L. Gradoń, Lattice-Boltzmann modeling of collisions between droplets and particles, Colloids & Surfaces A Physicochemical & Engineering Aspects, 441 (2014) 831-836.
[35] D. Zhang, K. Papadikis, S. Gu, Application of a high density ratio lattice-Boltzmann model for the droplet impingement on flat and spherical surfaces, International Journal of Thermal Sciences, 84 (2014) 75-85.
[36] K.A. Raman, R.K. Jaiman, T.S. Lee, H.T. Low, Lattice Boltzmann study on the dynamics of successive droplets impact on a solid surface, Chemical Engineering Science, 145 (2016) 181-195.
[37] J. Hyväluoma, J. Harting, Slip flow over structured surfaces with entrapped microbubbles, Physical Review Letters, 100 (2008) 246001.
[38] H. Li, C. Pan, C.T. Miller, Pore-scale investigation of viscous coupling effects for two-phase flow in porous media, Physical Review E Statistical Nonlinear & Soft Matter Physics, 72 (2005) 026705.
[39] Q. Li, Z. Chai, B. Shi, H. Liang, Deformation and breakup of a liquid droplet past a solid circular cylinder: a lattice Boltzmann study, Physical Review E Statistical Nonlinear & Soft Matter Physics, 90 (2014) 043015.
[40] Q. Li, K.H. Luo, Achieving tunable surface tension in the pseudopotential lattice Boltzmann modeling of multiphase flows, Physical Review E Statistical Nonlinear & Soft Matter Physics, 88 (2013) 053307.
[41] M.E. Mccracken, J. Abraham, Multiple-relaxation-time lattice-Boltzmann model for multiphase flow, Physical Review E Statistical Nonlinear & Soft Matter Physics, 71 (2005) 036701.
[42] R. Benzi, L. Biferale, M. Sbragaglia, S. Succi, F. Toschi, Mesoscopic modeling of a two-phase flow in the presence of boundaries: The contact angle, Phys Rev E Stat Nonlin Soft Matter Phys, 74 (2006) 021509.
[43] Q. Li, K.H. Luo, Q.J. Kang, Q. Chen, Contact angles in the pseudopotential lattice Boltzmann modeling of wetting, Phys.rev.e, 90 (2014) 053301.
[44] Q. Li, K.H. Luo, Thermodynamic consistency of the pseudopotential lattice Boltzmann model for simulating liquid–vapor flows, Applied Thermal Engineering, 72 (2014) 56-61.
[45] H. Huang, M. Krafczyk, X. Lu, Forcing term in single-phase and Shan-Chen-type multiphase lattice Boltzmann models, Physical Review E Statistical Nonlinear & Soft Matter Physics, 84 (2011) 046710.
[46] X. He, G.D. Doolen, Thermodynamic Foundations of Kinetic Theory and Lattice Boltzmann Models for Multiphase Flows, Journal of Statistical Physics, 107 (2002) 309-328.
[47] P.L. Li-Shi Luo, Theory of the lattice boltzmann method: dispersion, dissipation, isotropy, galilean invariance, and stability, Physical Review E Statistical Physics Plasmas Fluids & Related Interdisciplinary Topics, 61 (2000) 6546.
[48] Q. Li, Y.L. He, G.H. Tang, W.Q. Tao, Improved axisymmetric lattice Boltzmann scheme, Physical Review E Statistical Nonlinear & Soft Matter Physics, 81 (2010) 056707.
[49] Q. Li, K.H. Luo, X.J. Li, Lattice Boltzmann modeling of multiphase flows at large density ratio with an improved pseudopotential model, Phys Rev E Stat Nonlin Soft Matter Phys, 87 (2013) 053301.
[50] S. Mukherjee, J. Abraham, A pressure-evolution-based multi-relaxation-time high-density-ratio two-phase lattice-Boltzmann model, Computers & Fluids, 36 (2007) 1149-1158.
[51] P. Lallemand, L.S. Luo, Theory of the lattice boltzmann method: dispersion, dissipation, isotropy, galilean invariance, and stability, Physical Review E Statistical Physics Plasmas Fluids & Related Interdisciplinary Topics, 61 (2000) 6546-6562.
[52] P. Yuan, L. Schaefer, Equations of state in a lattice Boltzmann model, Physics of Fluids, 18 (2006) 329.

[53] M. Sbragaglia, R. Benzi, L. Biferale, S. Succi, K. Sugiyama, F. Toschi, Generalized lattice Boltzmann method with multirange pseudopotential, Physical Review E, 75 (2007) 026702.
[54] S. Fallah Kharmiani, M. Passandideh-Fard, H. Niazmand, Simulation of a single droplet impact onto a thin liquid film using the lattice Boltzmann method, Journal of Molecular Liquids, 222 (2016) 1172-1182.
[55] G.E. Cossali, M. Marengo, A. Coghe, S. Zhdanov, The role of time in single drop splash on thin film, Experiments in Fluids, 36 (2004) 888-900.
[56] A.L. Yarin, DROP IMPACT DYNAMICS: Splashing, Spreading, Receding, Bouncing…, Annual Review of Fluid Mechanics, 38 (2006) 159-192.
[57] X. He, Q. Zou, L.S. Luo, M. Dembo, Analytic solutions of simple flows and analysis of nonslip boundary conditions for the lattice Boltzmann BGK model, Journal of Statistical Physics, 87 (1997) 115-136.
[58] L. Courbin, J.C. Bird, M. Reyssat, H.A. Stone, Dynamics of wetting: from inertial spreading to viscous imbibition, J Phys Condens Matter, 21 (2009) 464127.
[59] K.G. Winkels, J.H. Weijs, A. Eddi, J.H. Snoeijer, Initial spreading of low-viscosity drops on partially wetting surfaces, Physical Review E Statistical Nonlinear & Soft Matter Physics, 85 (2012) 055301-055301.
[60] K. Sun, M. Jia, T. Wang, Numerical investigation of head-on droplet collision with lattice Boltzmann method, International Journal of Heat & Mass Transfer, 58 (2013) 260-275.
[61] H.K. Yong, W. Choi, J.S. Lee, Water droplet properties on periodically structured superhydrophobic surfaces: a lattice Boltzmann approach to multiphase flows with high water/air density ratio, Microfluidics & Nanofluidics, 10 (2011) 173-185.

Table.1 Comparison of the densities ρ_l and ρ_g obtained by numerical and Maxwell construction

	ρ_l / ρ_g			
T / T_c	Density ratio	Numerical	Maxwell construction	Reference [49]
0.8	12.82	3.13E-01/2.42E-02	3.14E-01/2.45E-02	-
0.75	21.84	3.332E-01/1.482E-02	3.32E-01/1.52E-02	-
0.7	38.41	3.58E-01/9.22E-03	3.58E-01/9.32E-03	-
0.65	67.46	3.822E-01/5.56E-03	3.832E-01/5.68E-03	-
0.6	135.40	4.062E-01/2.742E-03	4.062E-01/3.0E-03	4.077E-01/2.98E-03
0.55	293.20	4.3E-01/1.388E-03	4.31E-01/1.47E-03	4.317E-01/1.484E-04
0.5	750.83	4.542E-01/6.11E-04	4.55E-01/6.06E-04	4.559E-01/6.67E-04
0.48	1003.14	4.638E-01/4.43E-04	4.464E-01/4.45E-04	-

Figures

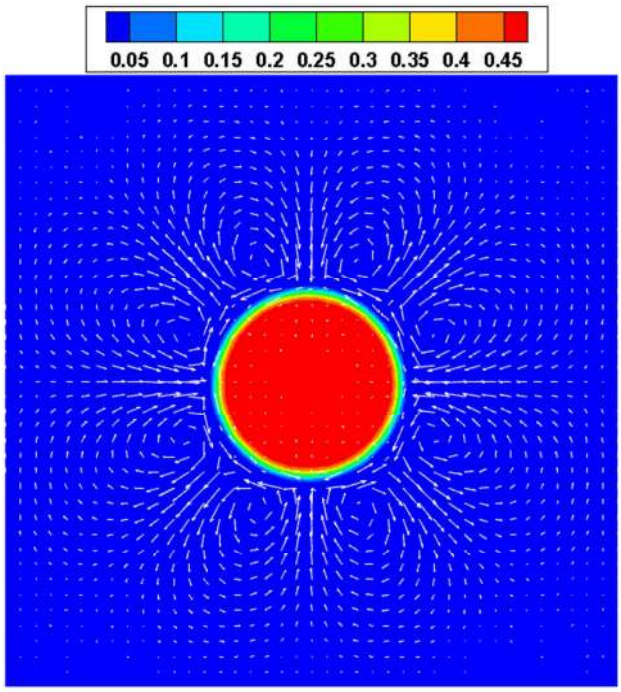

(a)

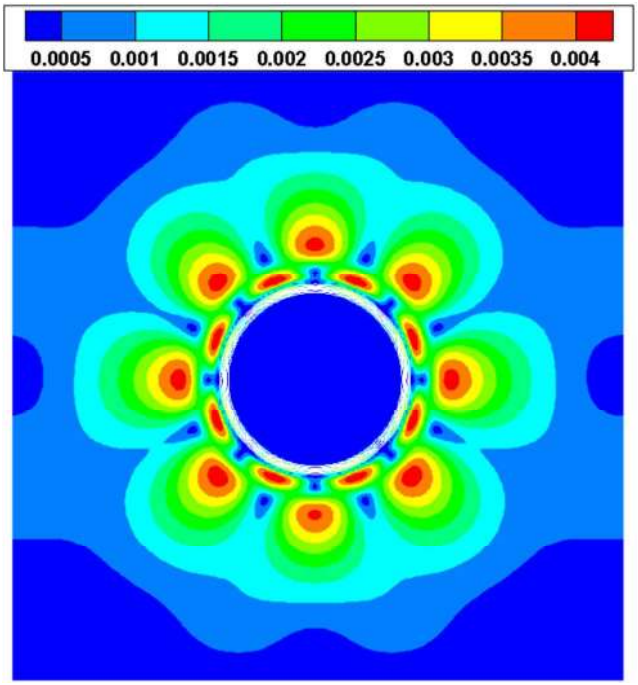

(b)

FIG. 1. Density distribution, spurious vector and spurious velocity contour around the droplet for DR of 1000(the top row (a) is density contour and velocity vector, the bottom row (b) is spurious velocity contour).

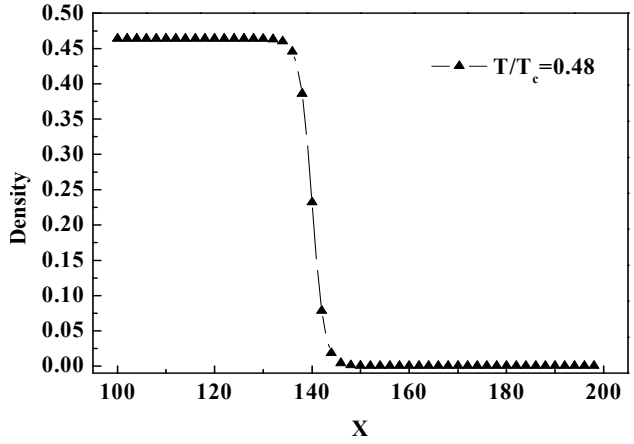

(a)

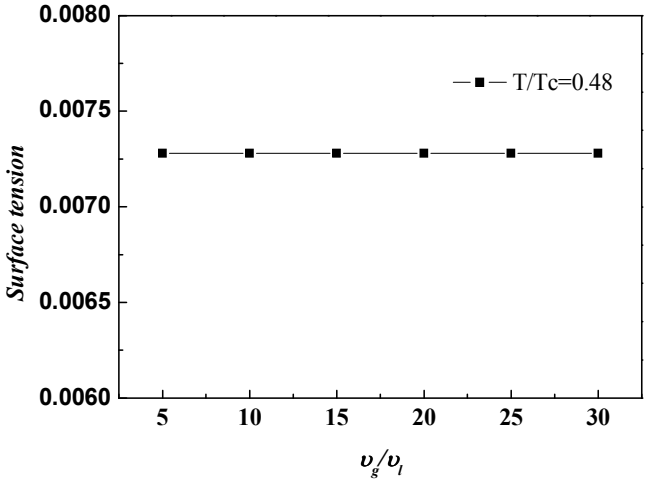

(b)

FIG. 2. (a): Gas-liquid density profile at the center line of Y-axis for DR of 1000, (b): relationship between the surface tension and KVR.

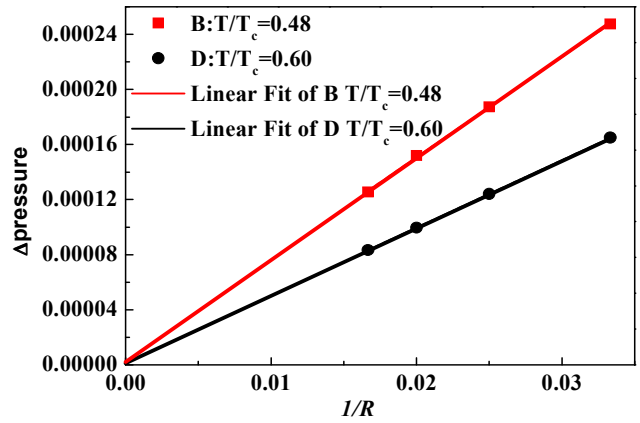

FIG. 3. Verification of the Laplace's law at two different density ratios.

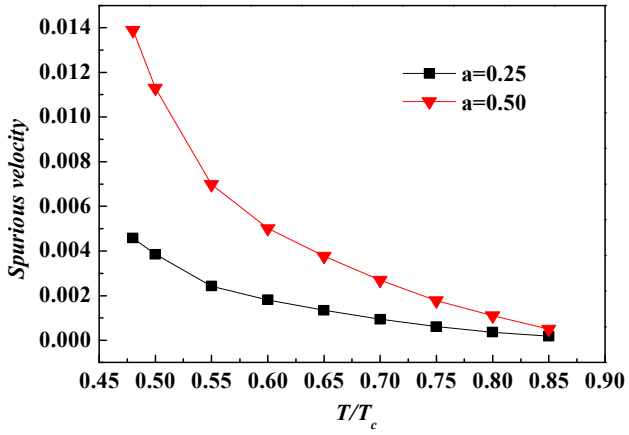

FIG. 4. Spurious velocity of different densities at different values of a=0.25, 0.5.

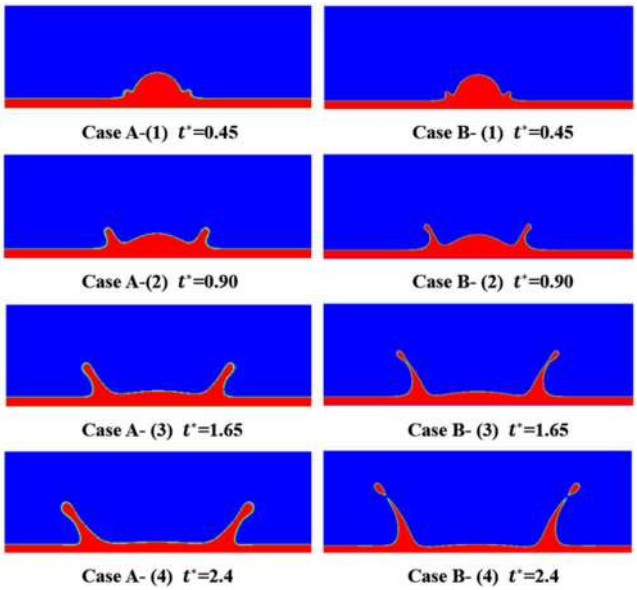

FIG. 5. Time evolution of droplet impact on a thin liquid film with DR of 750. The KVR is 5, We =180.63, Case A: Re =143.23, Case B: Re =1432.30.

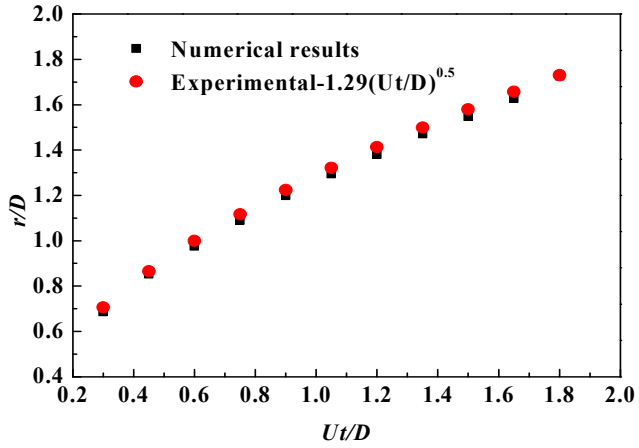

FIG. 6. Dimensionless crown radius versus DT with DR of 750 for Case B [55, 56].

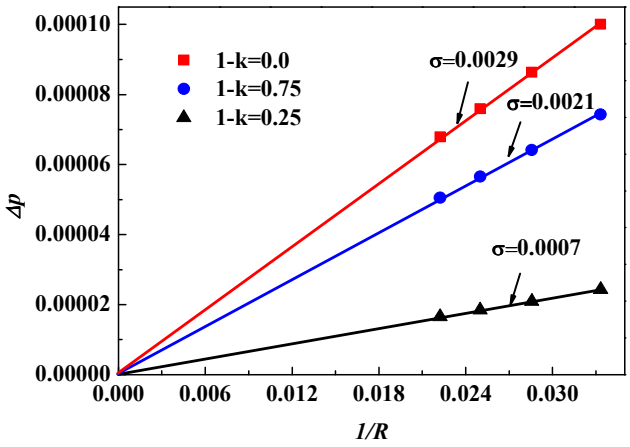

FIG. 7. Verification of the Laplace's law at different values of $1\text{-}k$.

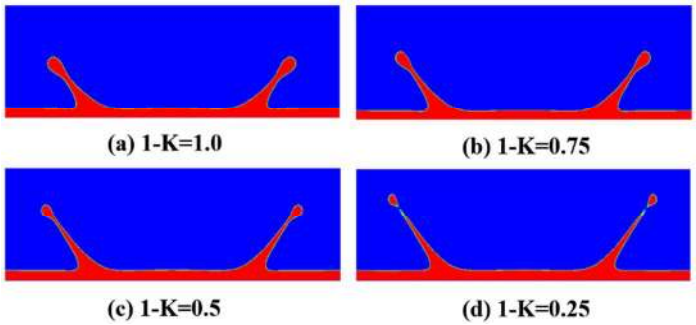

FIG. 8. Comparison of the density contours for different values of $1\text{-}k$ at t^* =2.64 (DR=750).

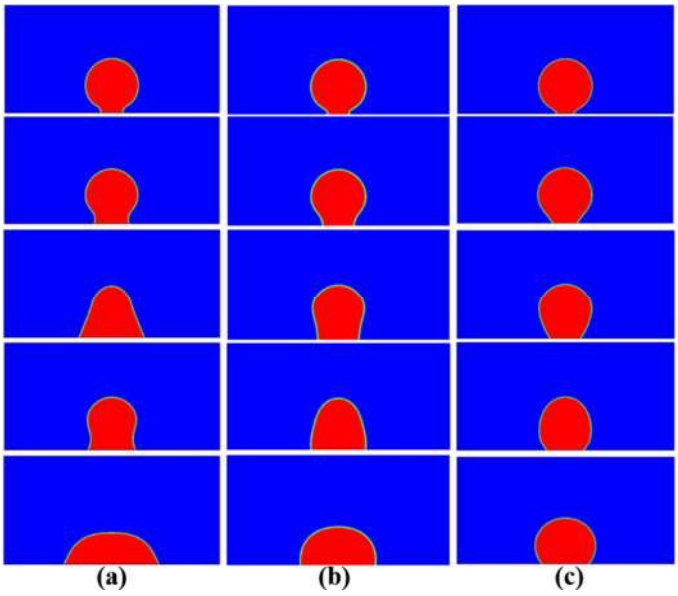

FIG. 9. The wetting process of stationary droplet at same time step with different Gw (Case a: Gw =-0.2, Case b: Gw =0.0,

Case c: Gw =0.2).

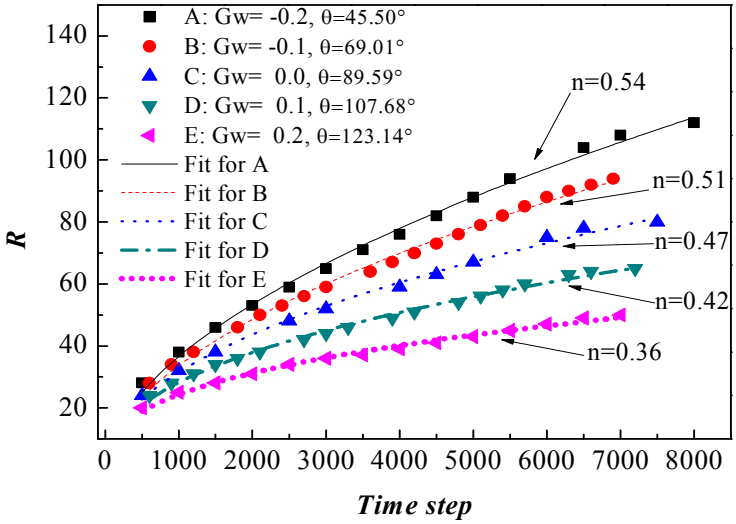

FIG. 10. Droplet spreading radius under different wetting walls over time.

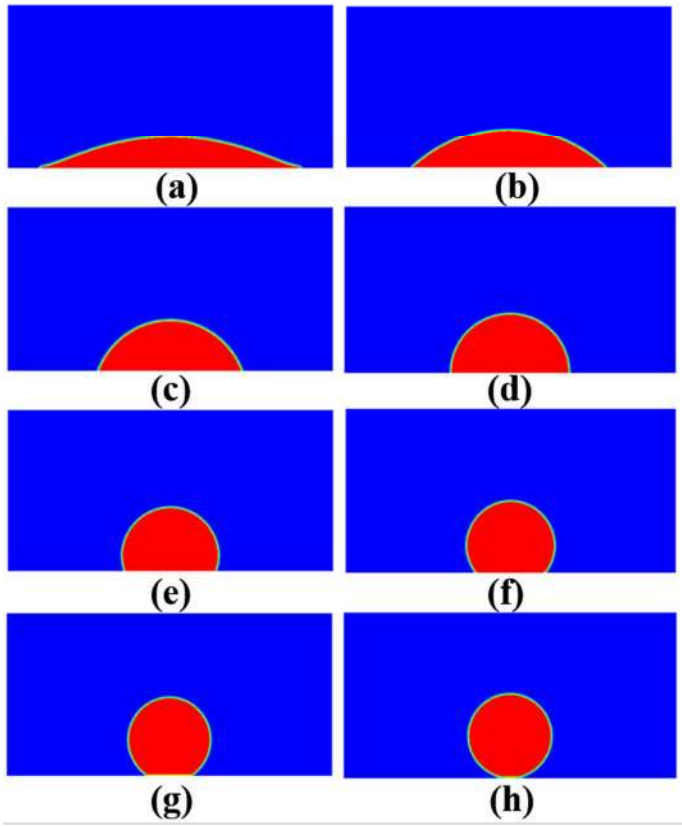

Fig. 11. Triple-phase contact line of the droplet on the wall at different Gw (Case a: Gw =-0.3, CA=19.25°, Case b: Gw =-0.2, CA=45.50°, Case c: Gw =-0.1, CA=69.01°, Case d: Gw =0.0, CA=90°, Case e: Gw =0.1, CA=107.68°, Case f: Gw =0.2, CA=123.14°, Case g: Gw =0.3, CA=140.80°, Case h: Gw =0.4, CA=163.85°).

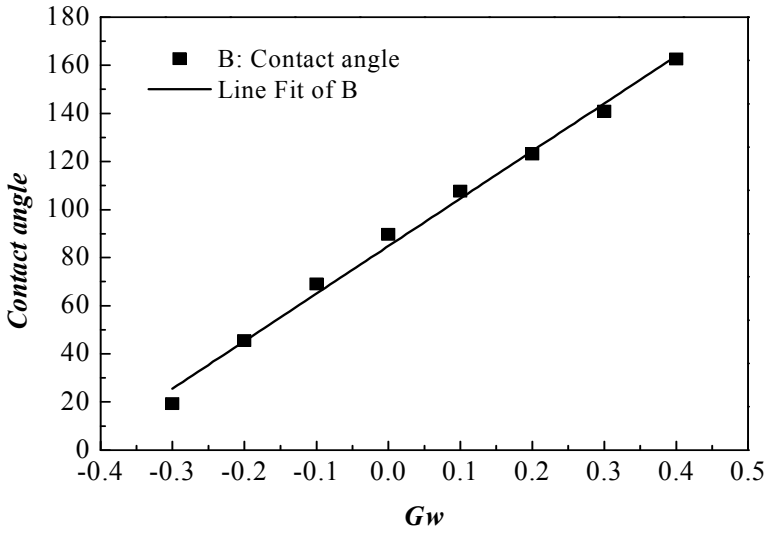

FIG. 12. Relationship between contact angle and Gw.

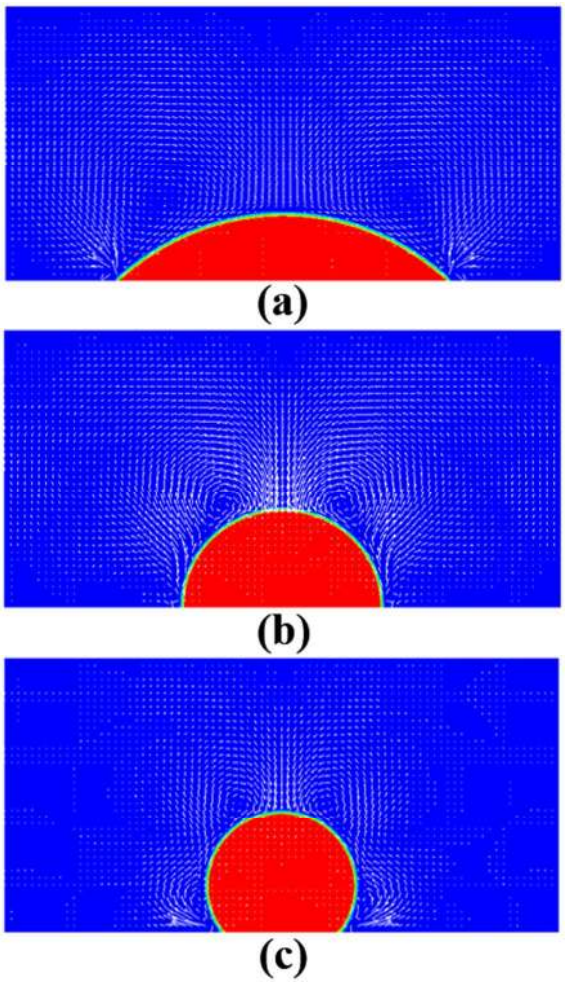

FIG. 13. The diagram of velocity vector of fluid at different wetting surface (Case a: CA=69.01°, Case b: CA=90°, Case c: CA= 107.68°).

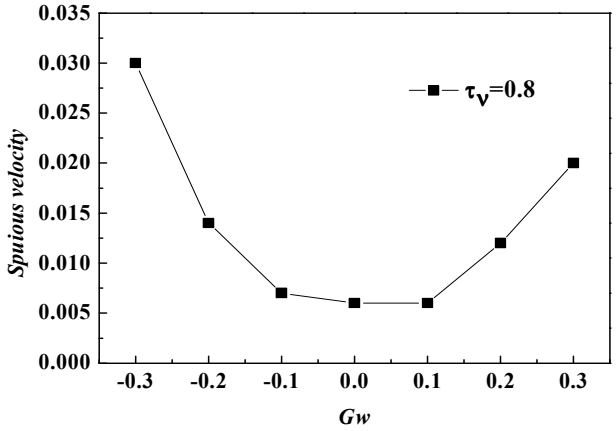

FIG. 14. The relationship between spurious velocity and Gw.

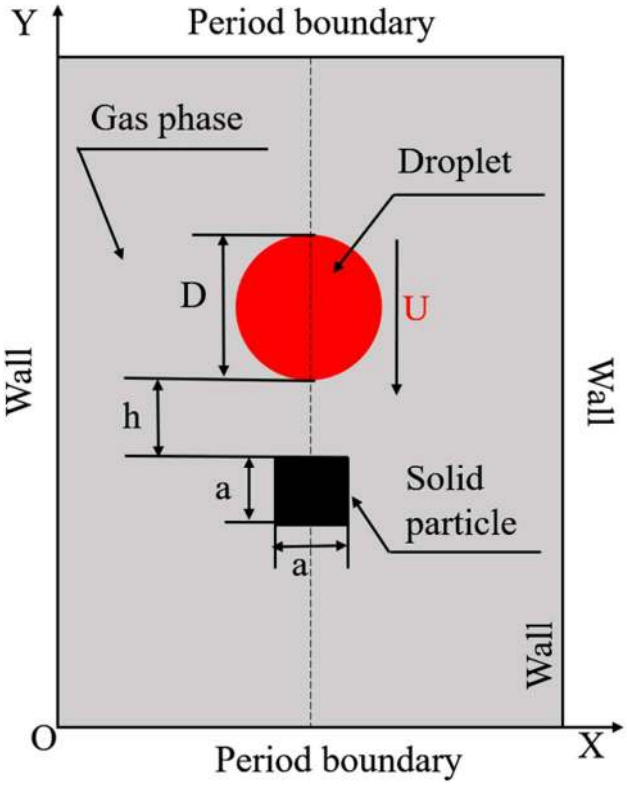

FIG. 15. Schematic of computational domain with droplet impact on solid particle along long channel.

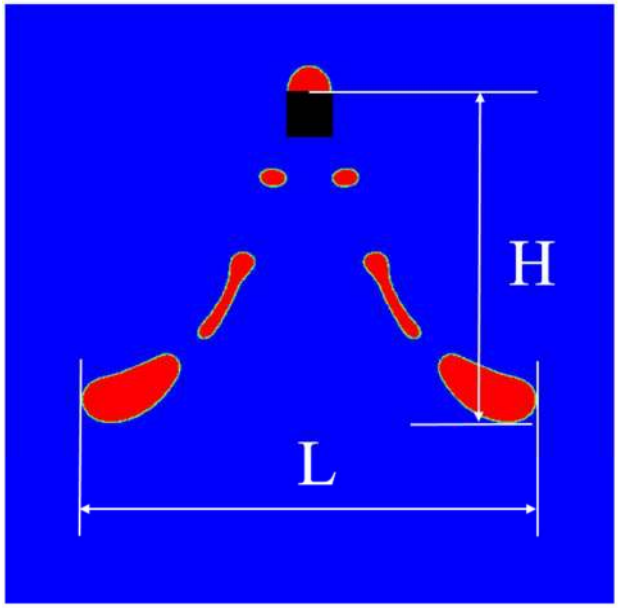

FIG. 16. Schematic of horizontal and vertical stretching length of liquid film after the droplet impacting solid.

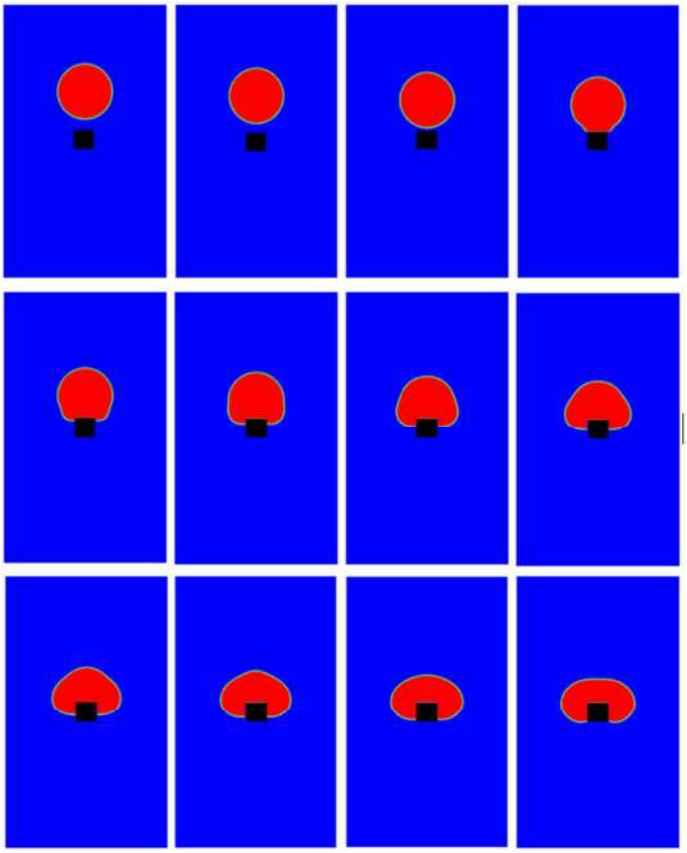

FIG. 17. Interface evolution over time during the droplet impacting on solid particle at DR=750, KVR=15, Re =300, We =4.32, CA=90°, the initial DT is T =0.08, and the DT step is ΔT =0.08.

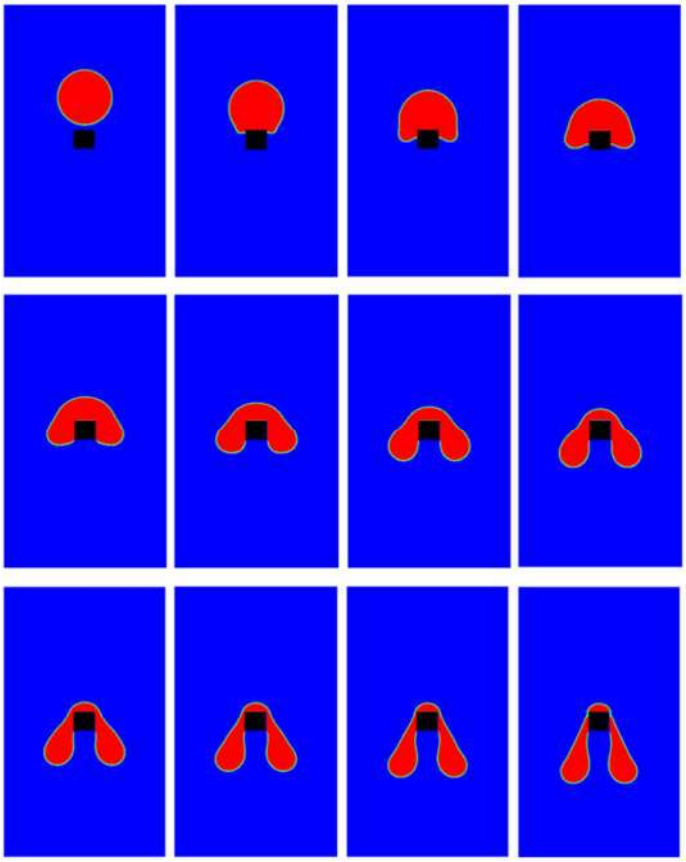

FIG. 18. Interface evolution of the droplet over time at DR=750, KVR=15, Re =750, We =27.03, CA=90°, the initial DT is T =0.2, and the DT step is ΔT =0.2.

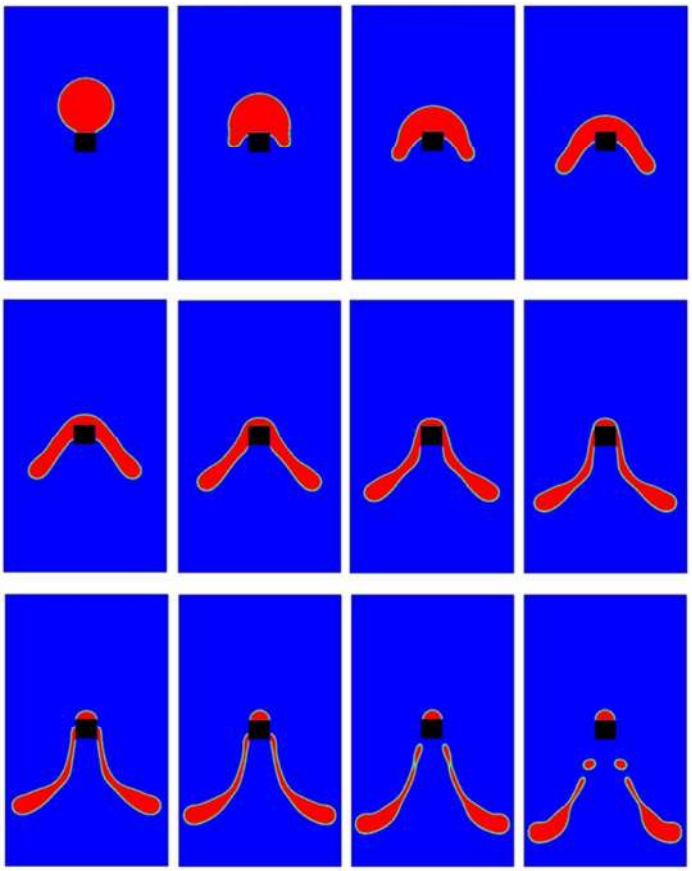

FIG. 19. Interface evolution of the droplet over time at DR=750, KVR=15, Re =1200, We =69.21, CA=90°, the initial DT is T =0.32, and the DT step is ΔT =0.32.

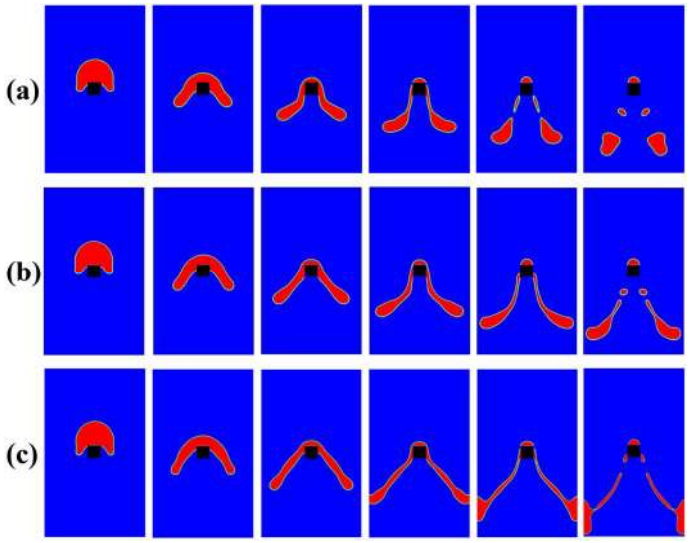

FIG. 20. The gas-liquid two-phase distribution under different We over time(Case a: We =44.72, Case b: We =69.21, Case c: We =145.34) at DR=750, KVR=15, Re =1200, CA=90°, the initial DT is T =0.64, and the DT step is ΔT =0.64.

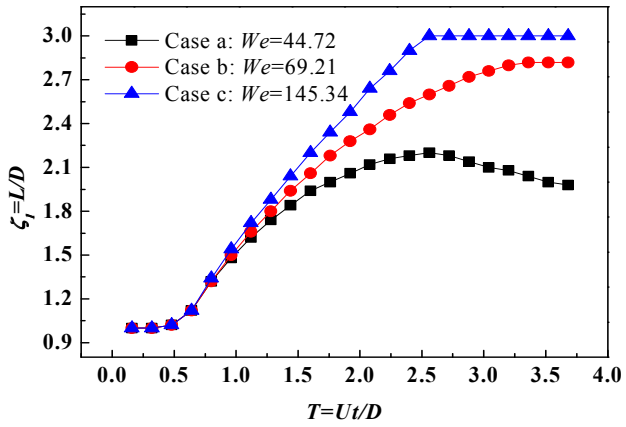

FIG. 21. The dimensionless expansion length versus DT of Case a: We =44.72, Case b: We =69.21, Case c: We =145.34 at DR=750, KVR=15, Re =1200, CA=90°.

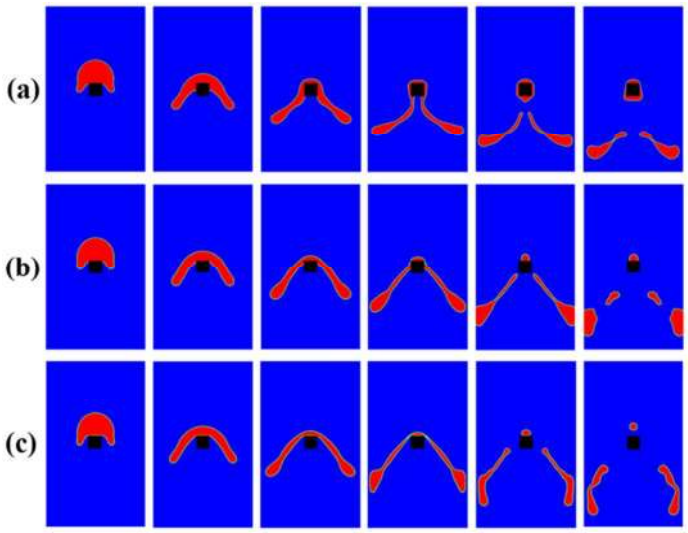

FIG. 22. Interface evolution of the droplet impacting on solid surface with different wetting property(Case a: CA=69.01°, Case b: CA=107.68°, Case c: CA=140.80°) at the same time at DR=750, KVR=15, Re =1200, We =69.21, the initial DT is T =0.64, and the DT step is ΔT =0.64.

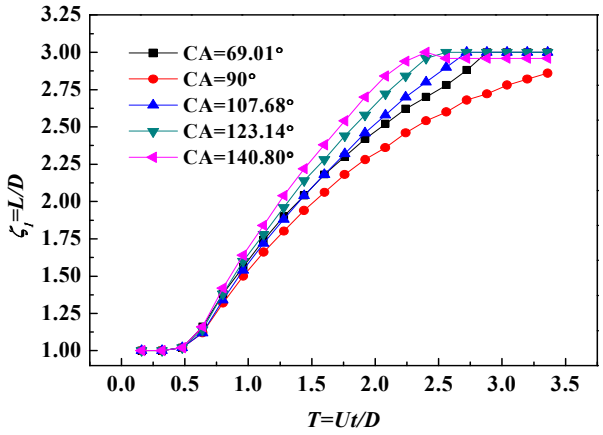

FIG. 23. The relationship between the dimensionless stretched length of the droplet in the horizontal direction and the non-dimensional time at different wetting walls at DR=750, KVR=15, Re =1200, We =69.21.

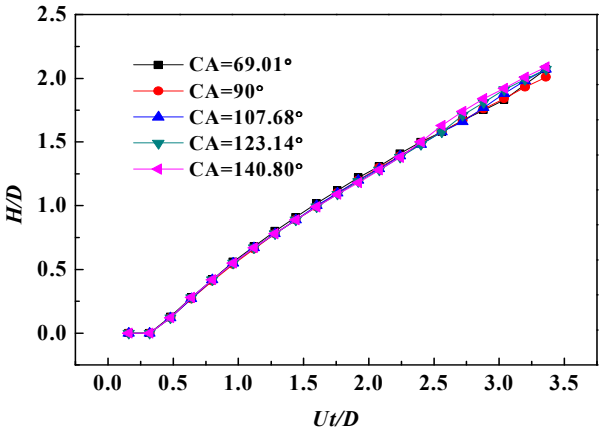

FIG. 24. The relationship between the dimensionless stretched length of the droplet in the vertical direction and the non-dimensional time at DR=750, KVR=15, Re =1200, We =69.21.

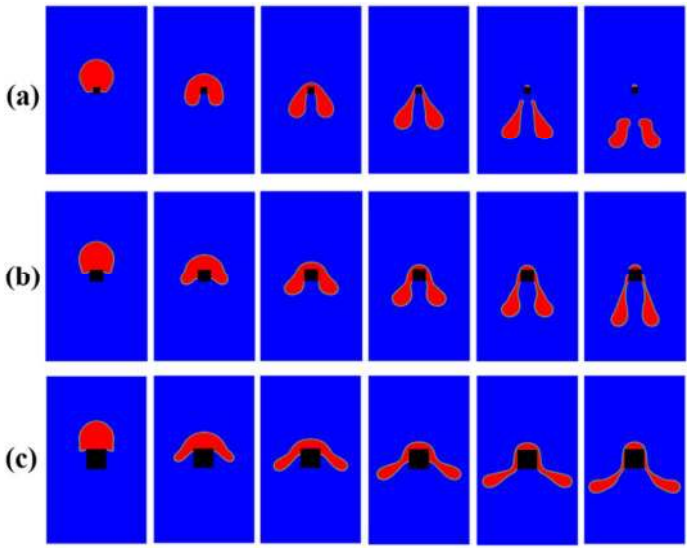

FIG. 25. Compassion of interface evolution at the same time for different solid partial size (Case a: χ_1=20/100, Case b: χ_1 =40/100, Case c: χ_1=60/100) at DR=750, KVR=15, Re=900, We=39, CA=90°, the initial DT is T=0.64, and the DT step is ΔT =0.64.

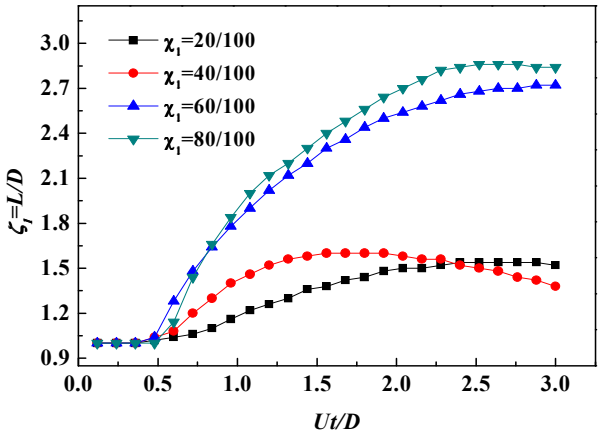

FIG. 26. the dimensionless horizontal expansion length versus DT at different solid particle sizes.

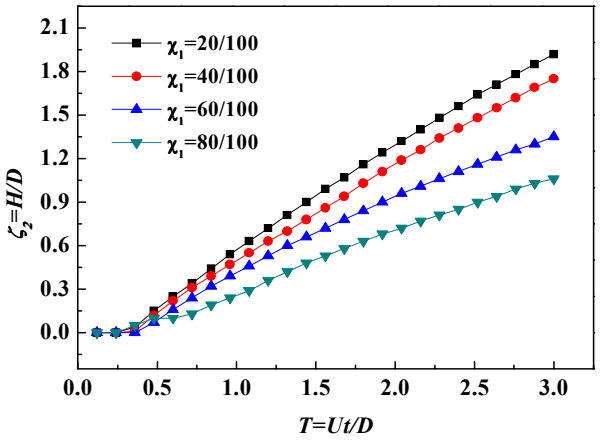

FIG. 27. the dimensionless vertical expansion length versus DT at different solid particle sizes.

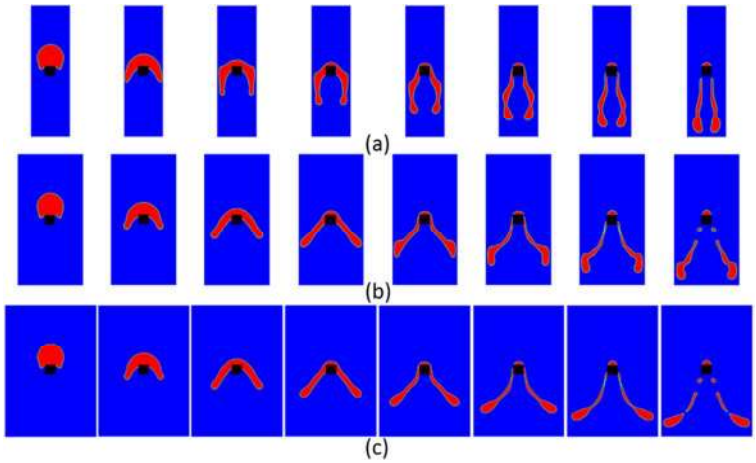

FIG. 28. Interface evolution of drop impacting on the solid particle at different width of the channel (case a: χ_2=150/100、case b: χ_2=250/100 and case c: χ_2=350/100) at the same DT of DR=750, KVR=15, Re=1200, We=69.21, CA=90°, the initial DT is T=0.48, and the DT step is ΔT=0.48.

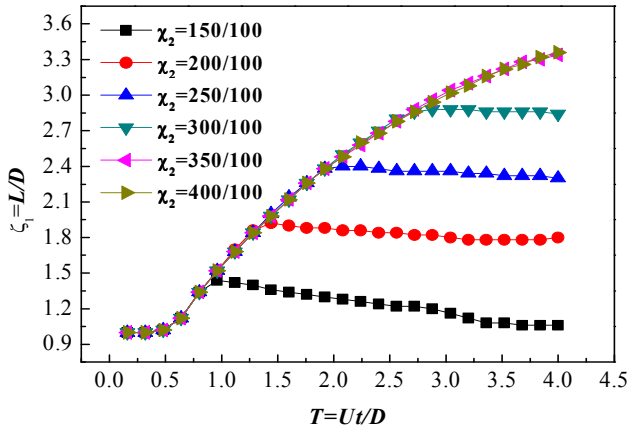

FIG. 29. Horizontal spreading dimensionless length versus DT at different microchannel width during the process of the droplet impacting.

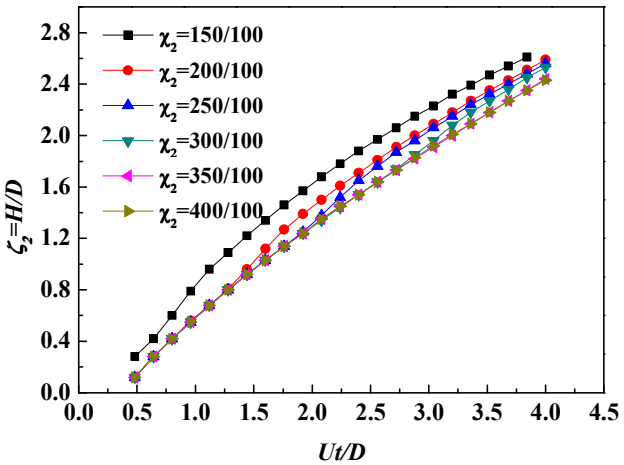

FIG. 30. Vertical spreading dimensionless length versus DT at different microchannel width during the process of the droplet impacting.

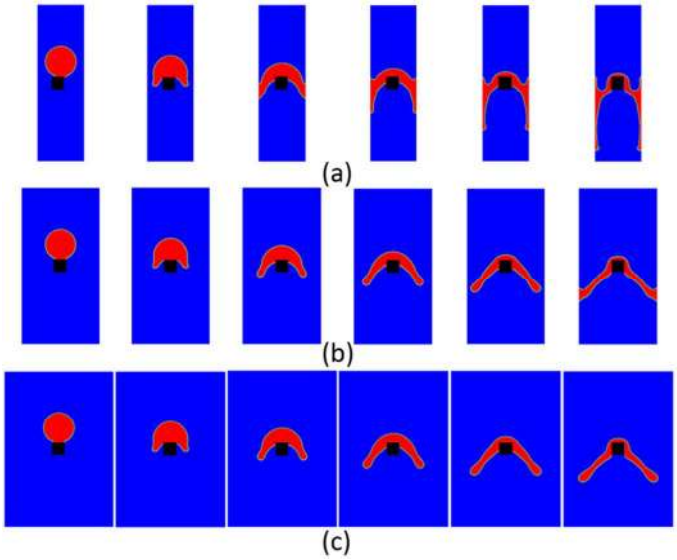

FIG. 31. Interface evolution under different width ratios of the channel (case a: χ_2=150/100、case b: χ_2=250/100 and case c: χ_2=350/100)during the droplet impacting and wetting the wall at the same DT of DR=750, KVR=15, Re=1200, We =69.21, CA=69.01°, the initial DT is T =0.32, and the DT step is ΔT =0.32.

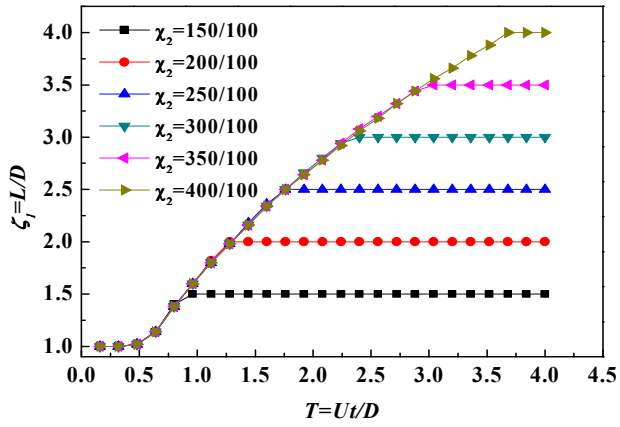

FIG. 32. Horizontal spreading dimensionless length verse DT at different microchannel width during the process of the droplet impacting.

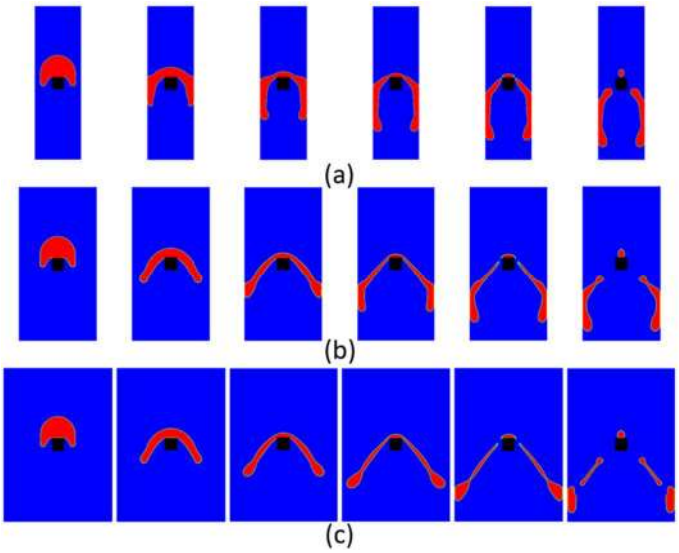

FIG. 33. Interface evolution under different width ratios(case a: χ_2=150/100、case b: χ_2=250/100 and case c: χ_2 =350/100) of the channel during the droplet impacting the solid particle at the same DT of DR=750, KVR=15, Re =1200, We =69.21, CA=123.14°, the initial DT is T =0.64, and the DT step is ΔT =0.64.

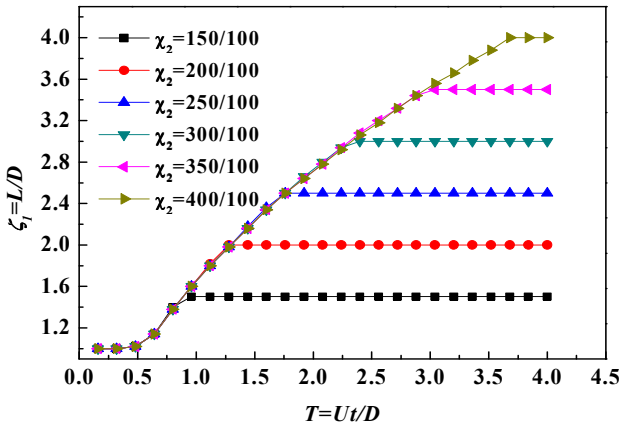

FIG. 34. The evolution process of horizontal spreading dimensionless length over DT under different widths of the channel.

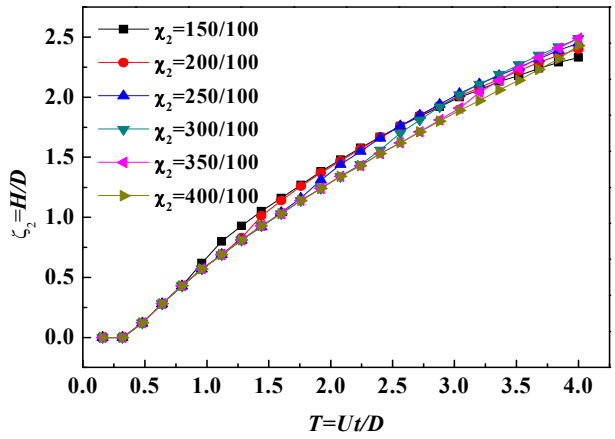

FIG. 35. The evolution process of vertical spreading dimensionless length over DT under different widths of the channel.